ALZHEIMER'S DISEASE

Inhibition of an Alzheimer's disease–associated form of necroptosis rescues neuronal death in mouse models

Marta J. Koper[1,2,3]†, Sebastiaan Moonen[1,2,3]†, Alicja Ronisz[1], Simona Ospitalieri[1], Zsuzsanna Callaerts-Vegh[4], Dries T'Syen[2,3], Sabine Rabe[5], Matthias Staufenbiel[5,6], Bart De Strooper[2,3,7]*‡, Sriram Balusu[2,3]*‡, Dietmar Rudolf Thal[1,8]*‡

Necroptosis is a regulated form of cell death that has been observed in Alzheimer's disease (AD) along with the classical pathological hallmark lesions of amyloid plaques and Tau neurofibrillary tangles. To understand the neurodegenerative process in AD, we studied the role of necroptosis in mouse models and primary mouse neurons. Using immunohistochemistry, we demonstrated activated necroptosis-related proteins in transgenic mice developing Tau pathology and in primary neurons from amyloid precursor protein (APP)–Tau double transgenic mice treated with phosphorylated Tau seeds derived from a patient with AD but not in APP transgenic mice that only exhibited β-amyloid deposits. Necroptosis proteins in granulovacuolar degeneration (GVD) bodies were associated with neuronal loss in mouse brain regions also known to be vulnerable to GVD in the human AD brain. Necroptosis inhibitors lowered the percentage of neurons showing GVD and reduced neuronal loss, both in transgenic mice and in primary mouse neurons. This suggests that a GVD-associated form of necroptosis that we refer to as "GVD-necroptosis" may represent a delayed form of necroptosis in AD. We propose that inhibition of necroptosis could rescue this type of neuronal death in AD.

INTRODUCTION

Alzheimer's disease (AD) is the most frequent neurodegenerative disorder leading to dementia (*1*). Neuropathologically, AD is characterized by two hallmark lesions: neurofibrillary tangles (NFTs) and amyloid plaques. NFTs are intraneuronal aggregates consisting of abnormally phosphorylated tau protein (pTau) (*2*), whereas amyloid plaques are extracellular deposits of the amyloid-β (Aβ) protein (*3*). Drugs targeting tau in AD are now in development but have not yet received approval (*4*). In contrast, the first drugs designed to target Aβ have recently been approved for the treatment of AD. Whereas these Aβ-targeting drugs have shown promise in reducing the amyloid load in the brain on the basis of amyloid positron emission tomography imaging, their effects on cognitive decline remain limited (*5*–*7*). When targeting Aβ, the neurodegenerative process slowed down but could not be fully stopped, despite amyloid plaque removal (*7*–*9*). Thus, preventing neuronal dysfunction and degeneration may be essential to stop cognitive impairment in patients with AD.

In the past 20 years, several regulated forms of cell death have been identified, among them necroptosis. Necroptosis, driven by necrosome assembly (*10*), has been associated with neuronal loss in AD (*11*, *12*). The necrosome is a protein complex involving the phosphorylated receptor–interacting protein kinase 1 (pRIPK1), which interacts with and phosphorylates RIPK3. pRIPK3 then activates mixed lineage kinase domain–like pseudokinase (MLKL) by phosphorylation. Once MLKL is phosphorylated, it oligomerizes, translocates to the plasma membrane, and forms pores to execute cell death (*13*).

In the AD brain, the necrosome does not primarily accumulate at the plasma membrane but in vacuoles and granules of lesions known as granulovacuolar degeneration (GVD) bodies (*12*). This form of necroptosis differs from canonical necroptosis that should be executed within a few hours (*14*), given that GVD-bearing neurons can nonetheless survive for a long time. GVD is a well-known degenerative lesion found in elderly brains as well as in AD brains (*15*, *16*). Predilection sites of GVD are the CA1 region of the hippocampus and the subiculum (*15*, *17*). However, the presence of GVD pathology in the amygdala and the frontal cortex is specifically associated with AD (*17*). Accordingly, GVD-mediated necroptosis pathway activation represents a pathological feature occurring in the AD brain, here referred to as GVD-necroptosis. This GVD-associated necroptotic neuronal degeneration depends on specific activation of the maternally expressed, imprinted long noncoding RNA gene 3 (MEG3), as demonstrated in a xenograft model of AD pathology (*18*). GVD in animal models has been reported in tau transgenic mice but not in amyloid precursor protein (APP) transgenic mice (*19*). However, it remains unclear whether tau transgenic animal models show a similar association with GVD-necroptosis as observed in the human brain (*12*) and in chimeric mice with xenotransplanted human neurons (*18*). Moreover, it is unknown whether AD-related neuron loss modeled in transgenic mice can be prevented by inhibiting necroptosis.

RESULTS

TAU22, TAU58, and APP23xTAU58 mice exhibit neuronal necroptosis pathway activation in GVD lesions associated with reduced neuronal density

To identify an animal model suitable for the investigation of the AD-associated necroptosis cell death pathway mediated by GVD pathology, we analyzed different mouse models of β-amyloidosis and tau pathology. These mouse models included heterozygous APP23, TAU22, TAU58,

[1]Laboratory for Neuropathology, Department of Imaging and Pathology, KU Leuven, Leuven Brain Institute (LBI), Leuven, Belgium. [2]Laboratory for the Research of Neurodegenerative Diseases, Department of Neurosciences, KU Leuven, Leuven Brain Institute (LBI), Leuven, Belgium. [3]Center for Brain and Disease Research, VIB, Leuven, Belgium. [4]Laboratory for Biological Psychology, KU-Leuven, Leuven, Belgium. [5]Novartis Institutes for Biomedical Sciences, Basel, Switzerland. [6]Department of Cellular Neurology, Hertie Institute for Clinical Brain Research, University of Tübingen, Tübingen, Germany. [7]UK Dementia Research Institute, University College London, London, UK. [8]Department of Pathology, University Hospital Leuven, Leuven, Belgium.
*Corresponding author. Email: dietmar.thal@kuleuven.be (D.R.T.); sriram.balusu@kuleuven.be (S.B.); bart.destrooper@kuleuven.be (B.D.S.)
†These authors contributed equally to this work.
‡These authors contributed equally to this work.

APP23xTAU58, and wild-type (WT) mice at 12 months of age (table S1). APP23 mice overexpress human APP carrying the Swedish double mutation (K670M/N671L) under the control of the neuron-specific murine Thy-1 promoter (*20*). TAU22 and TAU58 mice both overexpress human four-repeat tau carrying the P301S mutation driven by a Thy1.2 promoter (*21*, *22*). TAU22 mice carry a second G272V mutation. APP23xTAU58 mice were derived from cross-breeding APP23 and TAU58 mice (*23*). All mice had a C57Bl/6xBALB/c background (*22*). We detected a GVD-associated activation of the necroptosis pathway (GVD-necroptosis) in TAU22, TAU58, and APP23xTAU58 mice indicated by pMLKL-positive GVD bodies similar to those seen in human postmortem AD brain tissue (Fig. 1, A to I). GVD-necroptosis was predominantly found in neurons of the subiculum and CA1 mouse brain regions (Fig. 1, A to E; fig. S1; and table S2) (*12*). Further, affected areas were the amygdala, entorhinal cortex, and the neocortex (fig. S1 and table S2). GVD-associated necroptosis activation was not observed in the basal ganglia, the brain stem, or the cerebellum. APP23 transgenic mice did not show apparent GVD pathology or expression of pMLKL (Fig. 1, B and F, and fig. S1). All three necrosome components (pRIPK1, pRIPK3, and pMLKL) were found in these GVD lesions as shown in APP23xTAU58 mice (Fig. 2A). We confirmed their presence in GVD granules by costaining with casein kinase 1 delta (CK1δ), which is a standard marker for GVD pathology (Fig. 2, B and C) (*17*, *24*). Neuronal nuclei (NeuN) immunoreactivity confirmed the cellular identity of GVD-positive cells as neurons (Fig. 2, B and C). Using three-dimensional (3D) reconstructions, we observed that the majority of GVD granules were immunoreactive for both pMLKL and CK1δ. However, there were a few granules in the same GVD body that were positive for either pMLKL or CK1δ, whereas other granules in the same GVD body exhibited both proteins (Fig. 2C). Moreover, GVD vacuoles were often located close to the cell membrane, and affected neurons exhibited pyknotic nuclei indicative of ongoing cell death (Fig. 2D).

To compare the severity of GVD-necroptosis in the different mouse models, we quantified the percentage of neurons affected by GVD-necroptosis in the subiculum (Fig. 1, G to I). Here, 26.4% (± 1.6%) of the neurons in APP23xTAU58 mice exhibited pMLKL-positive GVD bodies compared with 0.9% (± 0.1%) of neurons in WT animals ($P < 0.001$; Fig. 1, A, E, and F). The percentage of neurons exhibiting GVD-associated necroptosis was also higher in tau transgenic animals compared with WT mice (TAU22, 12.3 ± 0.6%, $P < 0.001$; TAU58, 10.0 ± 2.0%, $P = 0.001$; Fig. 1, A, C, D, and F). Similar to WT mice, the mouse model of β-amyloidosis (APP23) exhibited almost no expression of the necrosome components at the age of 12 months (1.6 ± 0.2%, $P = 0.436$; Fig. 1, A, B, and F). Further, quantitative analysis of neuronal density in the subiculum (Fig. 1, G to I) revealed no significant neuronal reduction in APP23 mice (WT, 2122 ± 29.4 neurons/mm^2; APP23, 1984 ± 34.1 neurons/mm^2, $P = 0.315$; Fig. 1G). However, a strong decrease in neuronal density was observed in TAU22 (1752 ± 33.8 neurons/mm^2, $P = 0.001$) and TAU58 (1786 ± 43.95 neurons/mm^2, $P = 0.002$) mice, which was even more pronounced in APP23xTAU58 animals (1214 ± 36.4 neurons/mm^2, $P < 0.001$; Fig. 1G).

Using 12-month-old APP23xTAU58 mice, we carried out a similar quantitative analysis in a second mouse brain region, the amygdala (Fig. 3, A to D). The anatomical setting of the amygdala measurements is depicted in Fig. 3 (C and D). Similar to the subiculum, necroptosis activation and neuronal loss in the amygdala were observed in tau transgenic mouse models with or without β-amyloidosis, although the effects were less pronounced compared with the subiculum (Fig. 3, A and B). There was an increase in pMLKL-positive GVD-exhibiting neurons in the basolateral amygdala nuclei of APP23xTAU58 mice compared with those of WT mice ($P < 0.001$; Fig. 3A). This was accompanied by a reduced population of neurons (APP23xTAU58, 1186 ± 36.2 neurons/mm^2; WT, 1429 ± 54.7 neurons/mm^2, $P = 0.01$; Fig. 3B).

pTau pathology is a prerequisite for GVD-necroptosis

First, we analyzed the relationship between GVD-necroptosis and pTau aggregates in the subicula of 12-month-old APP23xTAU58 mice (fig. S2). pTau aggregates were detected with an antibody directed against pTau$^{S202/T205}$ (table S4) and defined as intraneuronal accumulation of pTau if covering at least one-third of a neuron. We detected pMLKL immunoreactivity in 55.8% of pTau-positive neurons in APP23xTAU58 mice (WT, 0.0 ± 0.0%; APP23xTAU58, 55.8 ± 2.1%, $P < 0.0001$; fig. S2). We also observed neurons positive for pTau that did not exhibit GVD-necroptosis (fig. S2). There were no GVD/pMLKL-positive neurons negative for pTau.

The overall distribution of pTau pathology in the different mouse lines affected the same regions in which GVD-necroptosis developed (fig. S1 and table S2). Aβ plaques were found in cortical (80%) and allocortical (40%) brain regions of 12-month-old APP23xTAU58 and APP23 mice (table S2). TAU22, TAU58, and WT mice showed no Aβ plaques (fig. S1 and table S2). Thus, GVD-necroptosis in TAU22 and TAU58 mice developed in the absence of Aβ.

Only single neocortical Aβ plaques were observed in 12.5% of 6-month-old APP23xTAU58 mice, whereas no plaques were found in 2-month-old APP23xTAU58 mice (table S2). In APP23xTAU58 mice, the number of affected brain regions exhibiting pMLKL-positive GVD pathology correlated with that of pTau-affected brain regions for the neocortex, entorhinal cortex, subiculum, CA1, and amygdala (Spearman correlation: $r = 0.93$, $P < 0.001$; analysis included APP23xTAU58 mice at 2, 6, and 12 months of age, $n = 19$ mice) and with the phase of Aβ plaque distribution established in APP transgenic mice (*25*) (Spearman correlation: $r = 0.78$, $P < 0.001$; analysis includes APP23xTAU58 mice at 2, 6, and 12 months of age, $n = 19$ mice). WT and APP23 mice showed no activation of the necroptosis pathway and no CK1δ-positive GVD bodies (table S2), indicating that Aβ pathology without pTau was not sufficient to drive GVD necroptosis. pTau pathology alone, however, was sufficient to induce GVD-necroptosis in TAU22 and TAU58 mice (table S2).

To investigate whether seeded tau aggregation in vitro also induced GVD-mediated necroptosis, we established an in vitro model by isolating primary hippocampal or cortical neurons from double transgenic mice (*App*$^{NL\text{-}G\text{-}F}$/*Tau22*$^{Tg/wt}$). On in vitro day 5, cells were treated with a sarkosyl-insoluble fraction of tau (Si-AD tau) isolated from a human brain with AD and analyzed for the presence of GVD-necroptosis markers using immunocytochemistry and the CellTiter-Glo assay to measure cell survival (fig. S3A). Around in vitro day 25, cells were fixed with methanol, and the neuronal cultures were analyzed. Cells from both cortical and hippocampal cultures displayed neuronal markers (MAP2) and mature presynaptic (SYNAPTOPHYSIN) and postsynaptic (HOMER) markers (fig. S3B). Around in vitro day 25, a reduction in cell viability was seen in the cortical and hippocampal neuronal cultures (Fig. 4A). Hippocampal cultures experienced a more pronounced loss of neurons when treated with Si-AD tau seeds. To confirm that the neurons in the hippocampal cultures underwent necroptosis, we used a necroptosis inhibitor necrostatin 1s (Nec-1s), which elicited rescue of neuronal loss after treatment with Si-AD tau seeds (fig. S3C). Despite the presence of

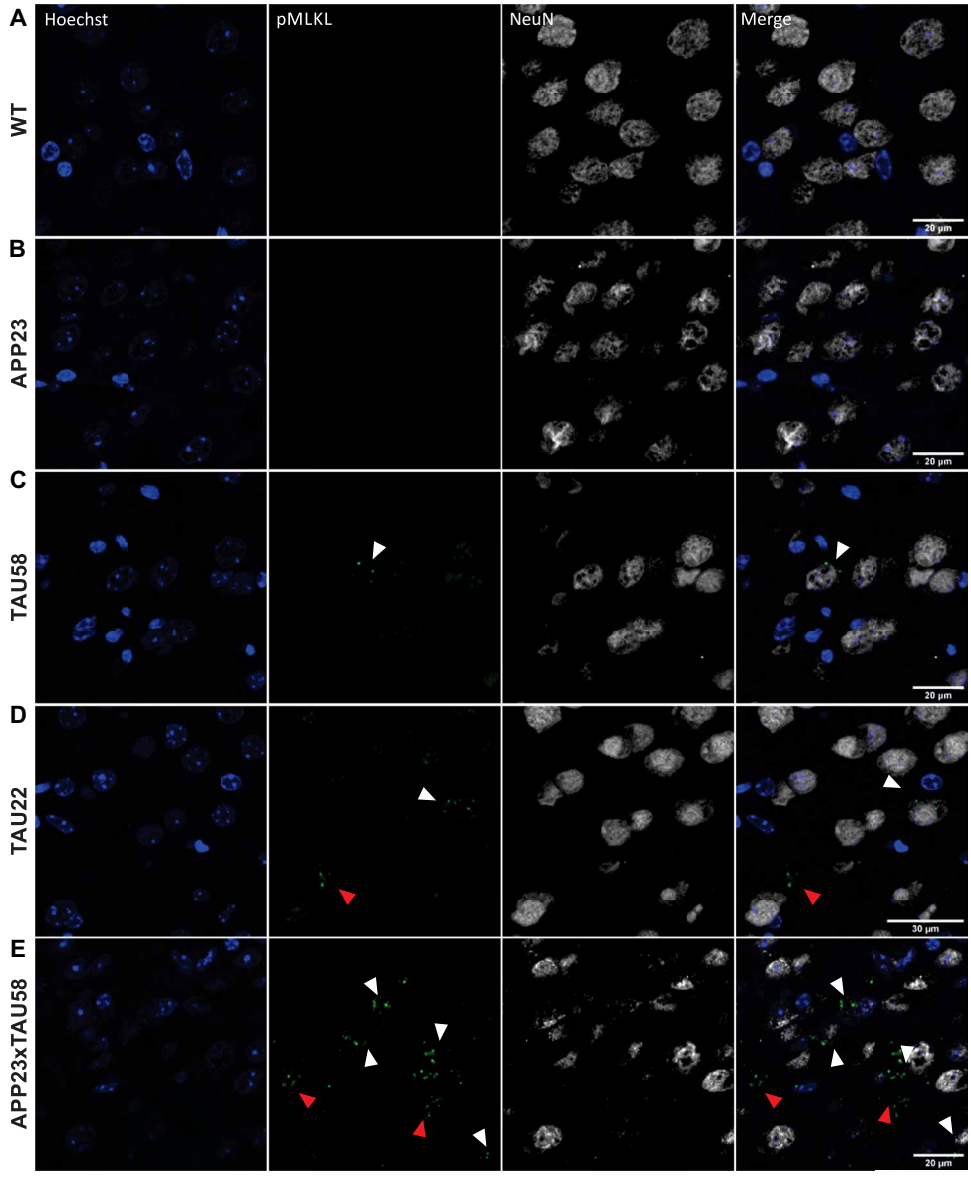

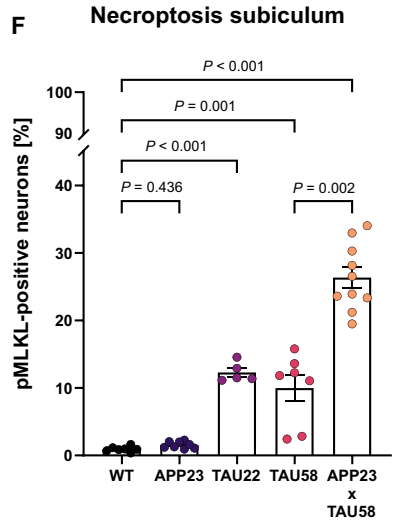

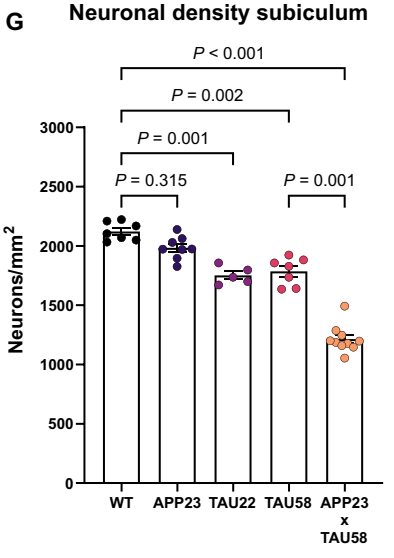

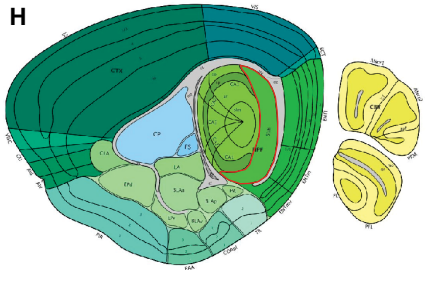

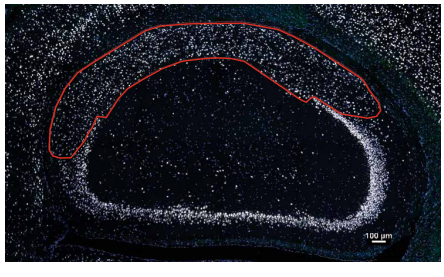

Fig. 1. GVD-associated necroptosis is associated with neuronal loss in mouse models of AD pathology. The brains of 12-month-old wild-type (WT; nontransgenic littermates), APP23, TAU58, TAU22, and APP23xTAU58 transgenic mice were sagittally cut and stained for immunofluorescence. (**A** to **E**) Representative confocal images show pMLKL staining (green, white arrowheads), neuronal nuclei (NeuN; gray), and Hoechst (blue) staining in the subicula of 12-month-old brains from WT mice (A), APP23 mice (B), TAU58 mice (C), TAU22 mice (D), and APP23xTAU58 mice (E). Scale bars, 20 µm. (**F**) Quantification of the necroptosis-positive neurons presented as a percentage of pMLKL-positive neurons relative to the total number of neurons. (**G**) Quantification of the neuronal density (neurons per square millimeter) in the subiculum based on the number of NeuN-positive neurons (gray). (**H**) Representative sagittal mouse brain section from the Allen brain atlas and (**I**) the corresponding representative confocal image used for quantifying necroptosis activation and neuronal loss. Subicular area used for the quantitative assessment is annotated in red. *P* values were controlled for sex using the Quade nonparametric ANCOVA test as shown in table S3; $P < 0.05$; WT, $n = 7$ animals; APP23, $n = 8$; TAU22, $n = 5$; TAU58, $n = 7$; APP23xTAU58, $n = 10$. Data are presented as mean ± SEM. Post hoc power analysis indicated a power of ≥99.6 % of the sample for comparisons among the different mouse models.

transgenic human four-repeat tau protein in the culture, only treatment with Si-AD tau seeds elicited robust tau aggregation, as indicated by immunoreactivity to the conformational tau epitope MC1 (Fig. 4B). MC1 recognizes the AD-associated paperclip formation of pTau (*26*), representing an advanced step in the maturation of pTau aggregates in AD (Fig. 4B) (*23*). Next, as observed in the mouse models with pTau pathology, we sought to validate the presence of an active necrosome complex and its association with GVD bodies. For this purpose, $App^{NL\text{-}G\text{-}F}/Tau22^{Tg/wt}$ transgenic mouse hippocampal cells from control and Si-AD tau–stimulated culture conditions were fixed with methanol and stained for activated necroptosis markers (pRIPK1, pRIPK3, and pMLKL) and the GVD marker casein kinase 1δ (CK1δ). All activated necroptosis markers displayed a punctuated pattern in the cell bodies of the neurons and colocalized with CK1δ (Fig. 4, C to

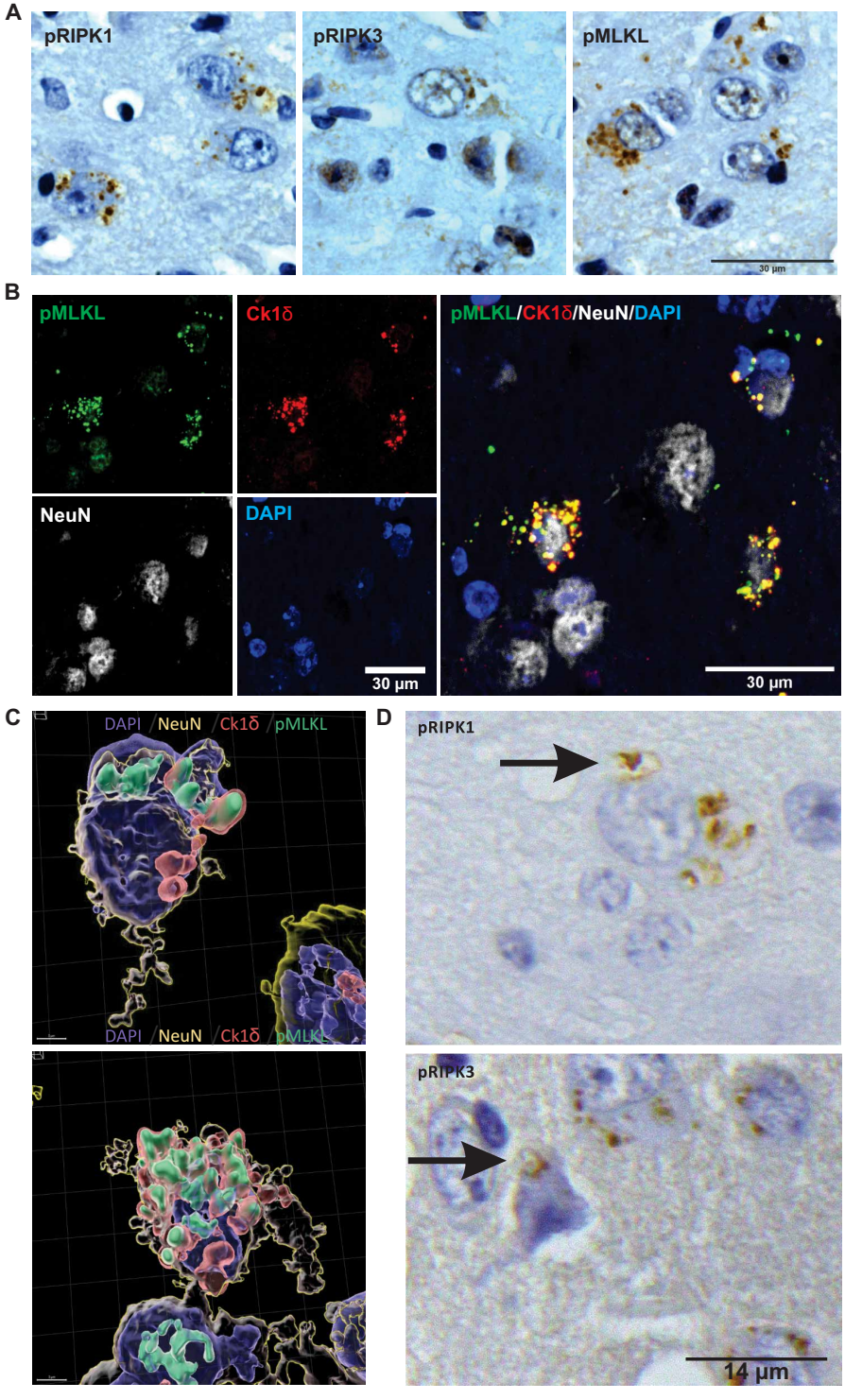

Fig. 2. GVD-associated necroptosis pathway is activated in the APP23xTAU58 mouse brain. (**A**) Diaminobecindine HCl–labeled immunostaining of APP23xTAU58 mouse brain sections was performed for the necrosome components pRIPK1, pRIPK3, and pMLKL (brown), and sections were counterstained using hematoxylin (blue). Scale bar, 30 μm. (**B**) Representative confocal images show immunofluorescence staining for pMLKL (green), GVD marker CK1δ (red), and neuronal marker NeuN (gray), together with 4′,6-diamidino-2-phenylindole (DAPI) for cell nuclei (blue) in the basolateral amygdalae of 12-month-old APP23xTAU58 mouse brains ($n = 10$). Scale bar, 30 μm. (**C**) Bitplane Imaris software was used for 3D modeling of mouse amygdala neurons. The presence of pMLKL (green) and CK1δ (red) is shown inside GVD bodies that surround NeuN (yellow). DAPI (purple) staining was performed to visualize general cell nuclei. Scale bar, 3 μm. (**D**) Representative bright-field microscope images show accumulation of pRIPK1-positive GVD (brown) at the plasma membrane of a subiculum neuron (black arrow) and pRIPK3-positive GVD (brown) in an amygdala neuron (black arrow) with pyknosis of the nucleus indicative of ongoing cell death. Scale bar, 14 μm.

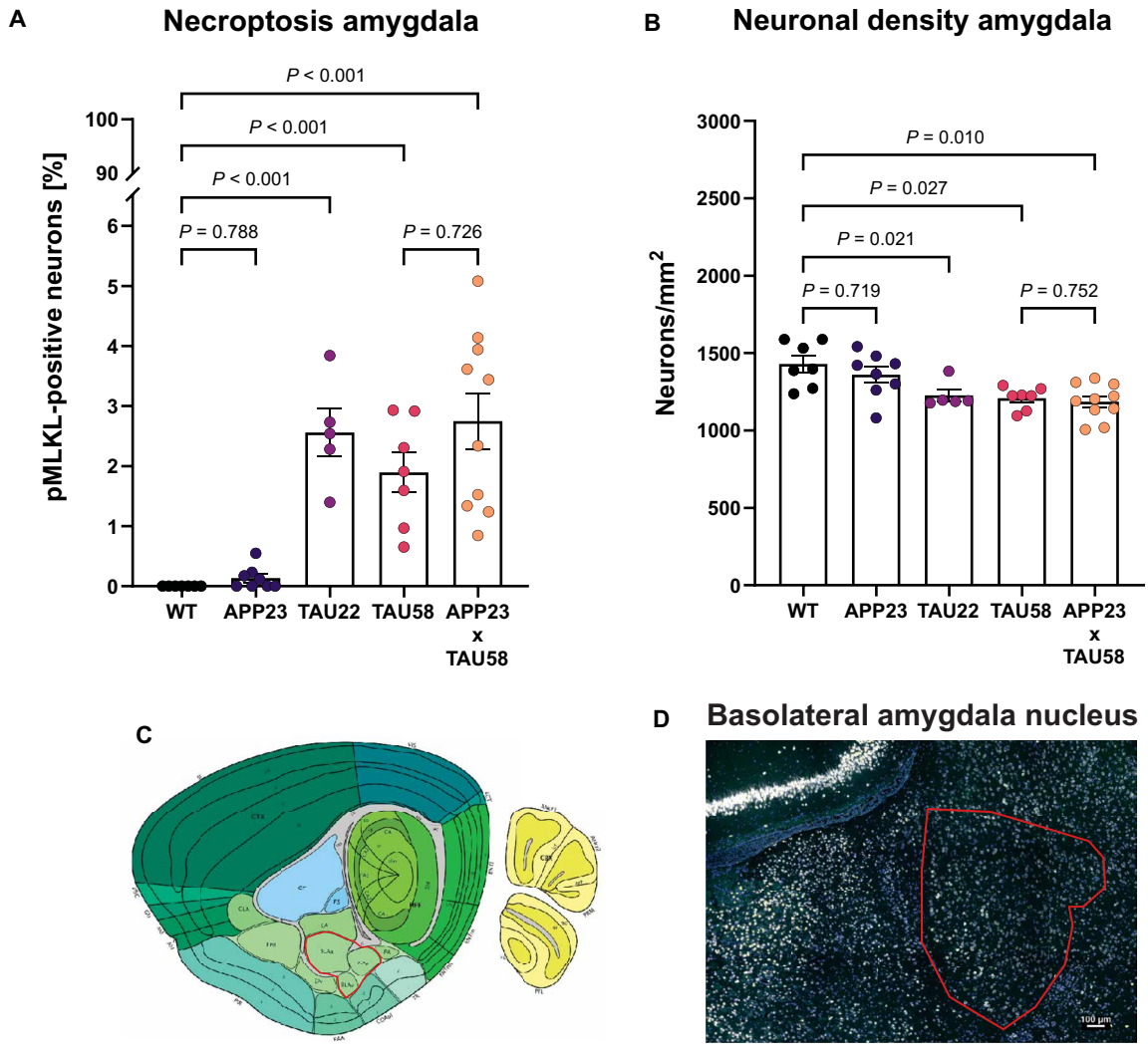

Fig. 3. Enhanced GVD-necroptosis in mouse amygdala neurons is inversely associated with neuronal density. Necroptosis activation and neuronal density were quantified in 12-month-old WT, APP23, TAU22, TAU58, and APP23xTAU58 mouse brains. (**A**) Necroptosis activation in the basolateral amygdala nuclei was quantified on the basis of the percentage of pMLKL-positive neurons relative to the total number of neurons. (**B**) Neuronal density was quantified as neurons per square millimeter based on the number of NeuN-positive neurons. (**C** and **D**) Shown is a representative sagittal mouse brain section from the Allen brain atlas (C) and the corresponding representative confocal image used for quantitative assessment (the annotated region of the basolateral amygdala nucleus is indicated in red) (D). Quade nonparametric ANCOVA was performed. *P* values were controlled for sex and are shown in table S3; $P < 0.05$; WT, $n = 7$ animals; APP23, $n = 8$; TAU22, $n = 5$; TAU58, $n = 7$; APP23xTAU58, $n = 10$. Data are presented as mean ± SEM. Post hoc power analysis indicated a power of ≥84.6% of the sample for comparisons among the different mouse models.

H, and fig. S3, D to F). Furthermore, intensity profile segmented areas (indicated with a red line in the Si-AD tau–stimulated conditions) from the necrosome-positive regions of the neurons demonstrated colocalization of CK1δ with necroptosis markers (pRIPK1, pRIPK3, and pMLKL) (Fig. 4, D, F, and H, and fig. S3G).

Inhibition of necroptosis with RIPK1/RIPK3 inhibitors prevents neuronal loss in APP23xTAU58 mice

Given the increase in GVD-necroptosis and the associated decrease in neuronal density in APP23xTAU58 mice compared with the other mouse models included in this study (Figs. 1 and 3), we selected APP23xTAU58 mice as the most suitable model for further neuropathological analyses as well as pharmacological interventions.

To find a specific time window for pharmacological intervention to inhibit the activation of the necroptosis pathway, we analyzed the expression of pMLKL-positive neurons together with the neuronal density in the subiculum and amygdala at two additional ages (2 and 6 months), in addition to 12-month-old APP23xTAU58 mice (Fig. 5). In 6-month-old animals, we observed a decreased neuronal density (WT, 2177 ± 87.8 neurons/mm^2; APP23xTAU58, 1812 ± 33.4 neurons/mm^2, $P < 0.0001$) and an increased percentage of pMLKL-positive neurons in the subiculum (WT, 0.9 ± 0.1%; APP23xTAU58, 6.4 ± 0.6%, $P < 0.0001$) (Fig. 5, A and B); this was not observed at 2 months of age (neuronal density: WT, 1999 ± 64.9 neurons/mm^2; APP23xTAU58, 2033 ± 34.1 neurons/mm^2 $P = 0.6406$; pMLKL-neurons: WT, 0.6 ± 0.1%; APP23xTAU58, 1.7 ± 0.3%, $P = 0.3765$) (Fig. 5, A and B). A similar analysis in basolateral amygdala nuclei showed consistent

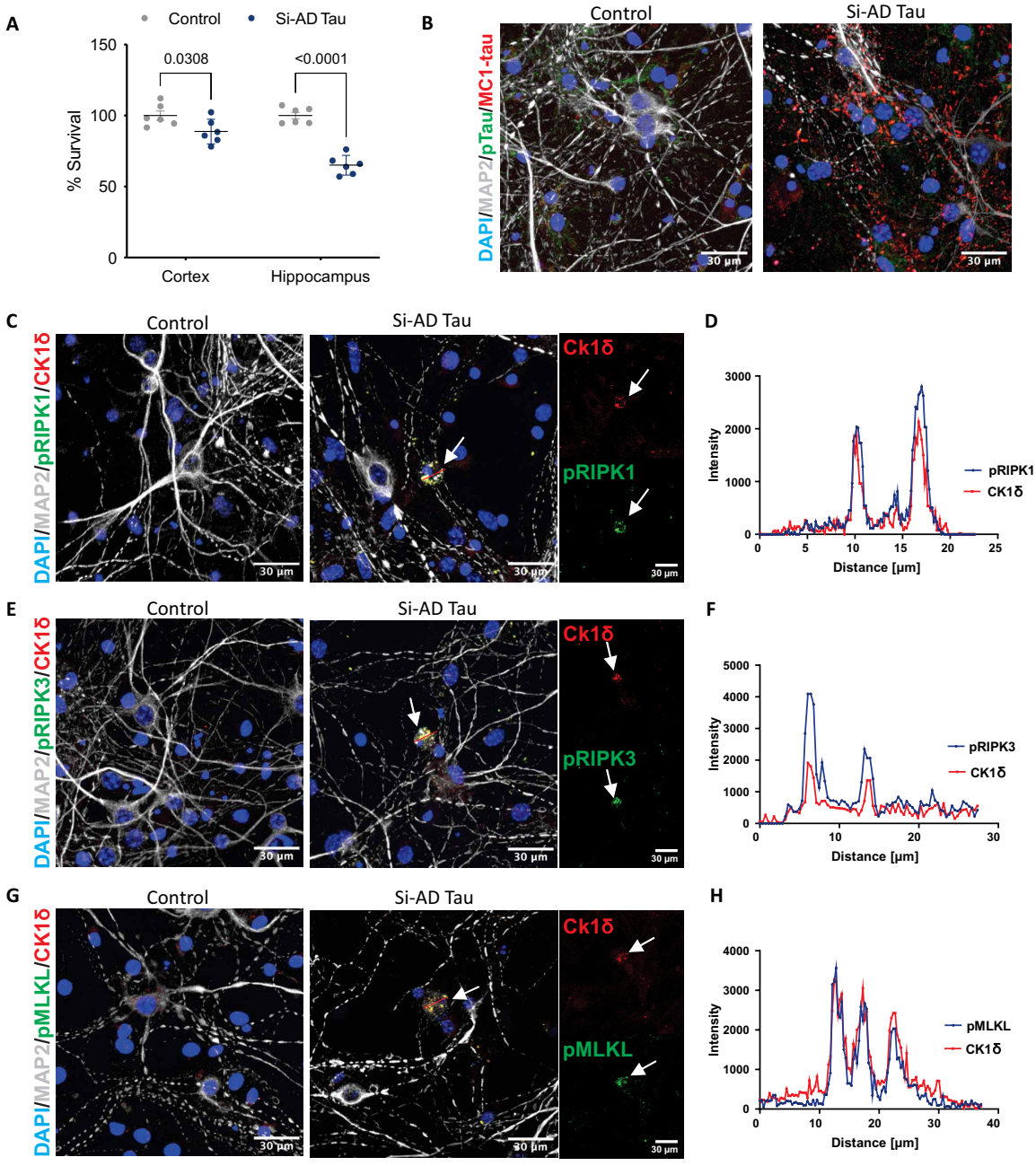

Fig. 4. Human AD brain–derived tau activates necroptosis in mouse neurons in vitro. Cortical and hippocampal neurons were derived from App$^{NL\text{-}G\text{-}F}$/Tau22$^{Tg/wt}$ mice and stimulated with Si-AD tau isolated from human postmortem brain tissue from a symptomatic AD case. (**A**) CellTiter-Glo assay (at approximately 20 days poststimulation) was performed to measure the percentage of surviving cells under control ($n = 6$ cultures from independent mouse embryos) compared with Si-AD tau seed–stimulated ($n = 6$ cultures from independent embryos) conditions for both cortical and hippocampal cultures. Two-way ANOVA with Bonferroni multiple comparisons test was used to determine statistical significance. (**B**) Representative confocal images of hippocampal neurons ($n = 7$ independent experiments) stained for pathological tau using the anti-pTau (AT8) antibody (green) and the MC1 antibody (red) against the paperclip formation of pTau. Scale bars, 30 µm. Representative confocal images ($n = 7$ independent experiments) show the colocalization between CK1δ and pRIPK1 (**C**), pRIPK3 (**E**), and pMLKL (**G**) in the mouse hippocampal cultures stimulated with Si-AD tau. Staining for MAP2 (gray), pRIPK1 (green), pRIPK3 (green) or pMLKL (green), and the GVD marker CK1δ (red) is shown. Scale bars, 30 µm. Staining intensity profiles show the colocalization between CK1δ (red) and pRIPK1 [(**D**), blue], pRIPK3 [(**F**), blue], and pMLKL [(**H**), blue]; colocalization is also indicated by the red lines and white arrows in (C), (E), and (G).

neuronal loss and necroptosis activation at 6 months but not at 2 months of age (Fig. 5, C and D). Overall, an age-related increase in GVD-necroptosis was observed on the basis of the pMLKL immunoreactivity in the subiculum and amygdala (Fig. 5E). Neuronal density and pMLKL-positive neurons strongly correlated with increasing age in APP23xTAU58 mice ($r = -0.955$, $P < 0.001$; $r = 0.938$, $P < 0.001$, respectively; table S6). At the age of 6 months, the APP23xTAU58 mouse model presented characteristics of both initial amyloidosis (12.5% of the animals in this experiment) and tauopathy (all animals) (*27*), whereas Aβ deposition was not observed at 2 months of age in

this model (table S2). To clarify whether neuron loss was accompanied by synapse loss or whether the synapse density remained stable despite neuron loss, we investigated the synapse density in the subicula of APP23xTAU58 mice. Quantification of synaptic density showed no significant changes at 6 ($P = 0.6236$) and 12 months ($P = 0.5655$) of age compared to WT animals (fig. S4).

To test the hypothesis that GVD-necroptosis leads to neuron death, which can be blocked by necroptosis inhibitors, we carried out a long-term treatment of APP23xTAU58 mice from 2 to 6 months of age. We used two different pharmacological inhibitors of RIPK1 and RIPK3: ponatinib (RIPK1 and RIPK3 inhibitors) and dabrafenib (RIPK3 inhibitor); these two inhibitors block other kinases as well (*28*). These drugs were chosen because they are already approved for use in humans without neurodegenerative conditions—ponatinib for chronic myeloid leukemia (*29*) and dabrafenib for malignant BRAF(V600)-mutant melanoma (*30*, *31*)—and are known to inhibit RIPK1 and RIPK3. Kaplan-Meier survival analysis showed no significant difference in survival probability between the treatment groups ($P = 0.3597$; fig. S5). None of the animals that died before the end of the experiment showed prior signs of illness. All animals included in the experiment showed GVD bodies exhibiting CK1δ, pRIPK1, pRIPK3, and pMLKL (Fig. 6, A to C, and fig. S6). CK1δ-positive GVD bodies lacking pRIPK1, pRIPK3, and pMLKL were not evident (fig. S6). A quantitative analysis of pMLKL immunoreactivity in the subicula of 6-month-old animals revealed a lower percentage of pMLKL-positive neurons in both drug-treated groups (ponatinib-treated, 2.0 ± 0.2%; dabrafenib-treated, 1.8 ± 0.2%) (Fig. 6D and table S7) compared with vehicle-injected APP23xTAU58 mice (vehicle treated, 6.6 ± 1.2%; ponatinib-treated, $P = 0.001$; dabrafenib-treated, $P < 0.001$) (Fig. 6D). Similarly, pRIPK1- and pRIPK3-positive GVD bodies were also decreased (Fig. 6E), confirming a decreased necrosome activation after ponatinib and dabrafenib treatment.

Next, we quantified the neuronal density in the subiculum and observed a higher neuronal density in the animals that received either the ponatinib or dabrafenib treatment (ponatinib-treated, 2111 ± 44.7 neurons/mm^2; dabrafenib-treated, 2086 ± 49.8 neurons/mm^2 compared with vehicle-injected APP23xTAU58 mice; vehicle-treated, 1769 ± 39.7 neurons/mm^2; ponatinib-treated, $P < 0.001$; dabrafenib-treated, $P < 0.001$) (Fig. 6F and table S7). Both drugs showed a similar effect ($P = 0.742$) in preventing neuronal loss.

In the basolateral amygdala nuclei, the treatment effect was less pronounced than in the subiculum (fig. S7). Only dabrafenib-treated animals showed a reduction in the number of pMLKL-positive neurons in the amygdala compared with vehicle-treated APP23xTAU58 mice (dabrafenib-treated, 1.2 ± 0.3%; vehicle-treated, 2.3 ± 0.3%; $P = 0.012$) (fig. S7A). Similar to the subiculum, neuronal density was increased in both the ponatinib-treated and dabrafenib-treated animals compared with vehicle-treated APP23xTAU58 animals (ponatinib-treated, 1342 ± 34.4 neurons/mm^2; dabrafenib-treated, 1328 ± 34.24 neurons/mm^2; vehicle-treated, 1222 ± 28.38 neurons/mm^2; ponatinib-treated, $P = 0.007$; dabrafenib-treated, $P = 0.013$ compared with vehicle-treated animals) (fig. S7B). Group differences were controlled for sex (table S7). Last, the distribution of pMLKL-exhibiting GVD lesions was less widespread among CA1, subiculum, amygdala, entorhinal cortex, and neocortex in ponatinib-treated and dabrafenib-treated animals compared with vehicle-treated animals (binary logistic regression analysis controlled for Aβ phase and pTau distribution: $P = 0.032$; odds ratio: 0.219; 95% confidence interval: 0.055 to 0.875) (fig. S7 and table S9).

To further clarify the drug treatment effects on the neurodegenerative process, we investigated the synapse density and pTau load in the subiculum (fig. S8). Subicular pTau load was not changed in ponatinib-treated ($P = 0.6365$) or dabrafenib-treated mice ($P = 0.7223$) compared to vehicle-injected animals (fig. S8, A and D). Likewise, the densitometrically measured synapse density in the subiculum did not change after treatment with ponatinib ($P = 0.6253$) or dabrafenib ($P = 0.9534$) compared to vehicle-injected mice (fig. S8, B and E). No subicular Aβ deposits were detected (fig. S8C).

Inhibition of necroptosis improves cognitive function of APP23xTAU58 mice

To clarify the functional impact of GVD-necroptosis and its inhibition in dabrafenib-treated and ponatinib-treated 6-month-old APP23xTAU58 mice, we performed a fear conditioning test, a working memory assessment in the T-maze, and a social recognition test (Fig. 7). Whereas all animals showed normal social interest (Fig. 7A), social recognition memory was improved in ponatinib-treated and dabrafenib-treated APP23xTAU58 mice in contrast with vehicle-injected mice (Fig. 7B). Two-way analysis of variance (ANOVA) for factor side indicated a significant effect [$F(1,60) = 16.73$, $P = 0.0001$], and post hoc contrast analysis confirmed that both treatments increased preference for a newly introduced (stranger) mouse (Šidák multiple comparisons of the first stranger animal S1 versus the second stranger animal S2: ponatinib-treated APP23xTAU58, $P = 0.0118$; dabrafenib-treated APP23xTAU58, $P = 0.0409$; Fig. 7B). In contrast, neither working memory nor fear conditioning showed evident differences among the groups (Fig. 7, C and D). During working memory assessment in the T-maze (Fig. 7C), time spent in either goal arm was similar, and no preference for the previously unknown arm over the familiar arm was observed {effect for arm [$F(1,60) = 0.2285$, $P = 0.6344$]}. When compared to a neutral context, all animals showed context A–specific (environment to which the animals were habituated at the start of the experiment) and conditioned stimulus-specific memory (Fig. 7D). Two-way ANOVA indicated a significant effect for phase [$F(2,132) = 42.34$, $P < 0.0001$] but not for group [$F(2,132) = 2.410$, $P = 0.0938$] or interaction.

DISCUSSION

The results of the current study support our hypothesis of the existence of a pathological, delayed form of necroptosis, which is associated with GVD. Recent findings indicate that necroptosis is a key mechanism driving neuronal death in mouse models of AD pathology (*11*, *32*). GVD-associated necroptosis was observed in human xenograft mouse models of AD pathology (*18*). The presence of GVD-necroptosis in TAU22, TAU58, and APP23xTAU58 mice extends the initial findings by Balusu *et al.* (*18*, *33*) by demonstrating the involvement of neurons in the same brain regions reported in the AD brain: the subiculum, amygdala, and cortex (*12*, *17*, *34*, *35*). Morphologically, necroptosis activation in these mice resembled GVD-necroptosis in postmortem brain tissue from human AD cases (*12*). In addition, GVD-necroptosis and associated neuronal loss selectively affected mouse models with tau pathology and primary mouse neurons treated with pathological tau, in line with previous reports (*18*, *19*, *36*, *37*), but not mouse models with β-amyloidosis alone, such as the APP23 mice. Pharmacological inhibitors targeting the necroptosis proteins RIPK1 and RIPK3 prevented the loss of neurons in the APP23xTAU58 mouse model and improved social

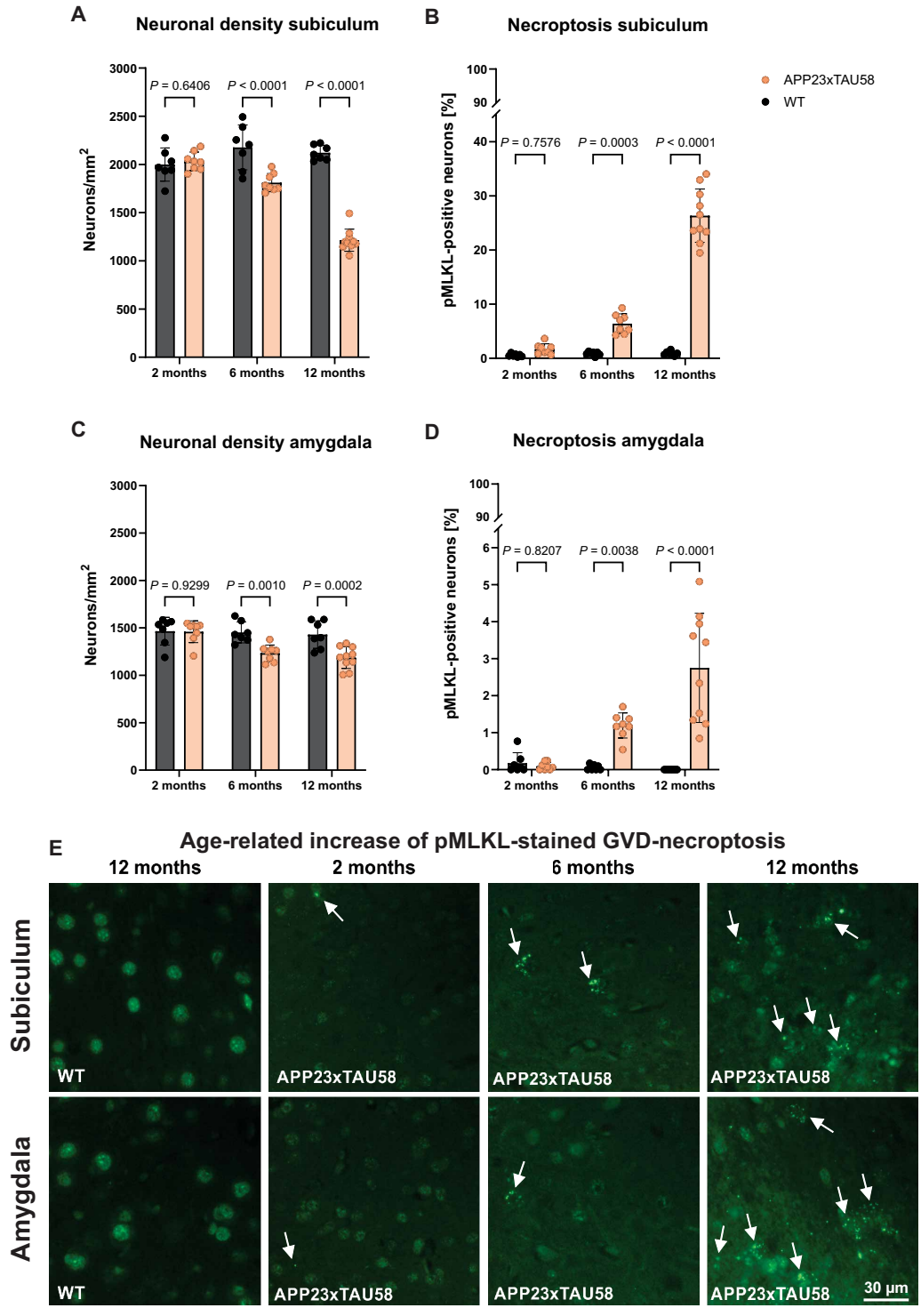

Fig. 5. Neuron loss and GVD-necroptosis increases in severity with age in APP23xTAUA58 mice. Neuronal density and necroptosis activation were quantified in 2-, 6-, and 12-month old APP23xTAU58 and WT mice. Neuronal density was quantified as neurons per square millimeter on the basis of the number of NeuN-positive neurons in the subiculum (**A**) and basolateral amygdala nucleus (**C**). Necroptosis activation was quantified on the basis of the percentage of pMLKL-positive neurons relative to the total number of neurons in the subiculum (**B**) and in the basolateral amygdala nucleus (**D**). (**E**) Representative images of 12-month-old WT mouse brains and 2-, 6-, and 12-month-old APP23xTAU58 mouse brains stained for pMLKL in the subiculum (top) and the amygdala (bottom). Scale bar, 30 µm. Two-way ANOVA [(A) and (B)] or Mann-Whitney [(C) and (D)] was performed showing uncorrected *P* values; *P* values corrected for multiple testing are found in table S5; $P < 0.05$; WT mice, $n = 7$; APP23xTAU58 mice, $n = 8$ (2 and 6 months) and $n = 10$ (12 months) per age group. Data are presented as mean ± SEM.

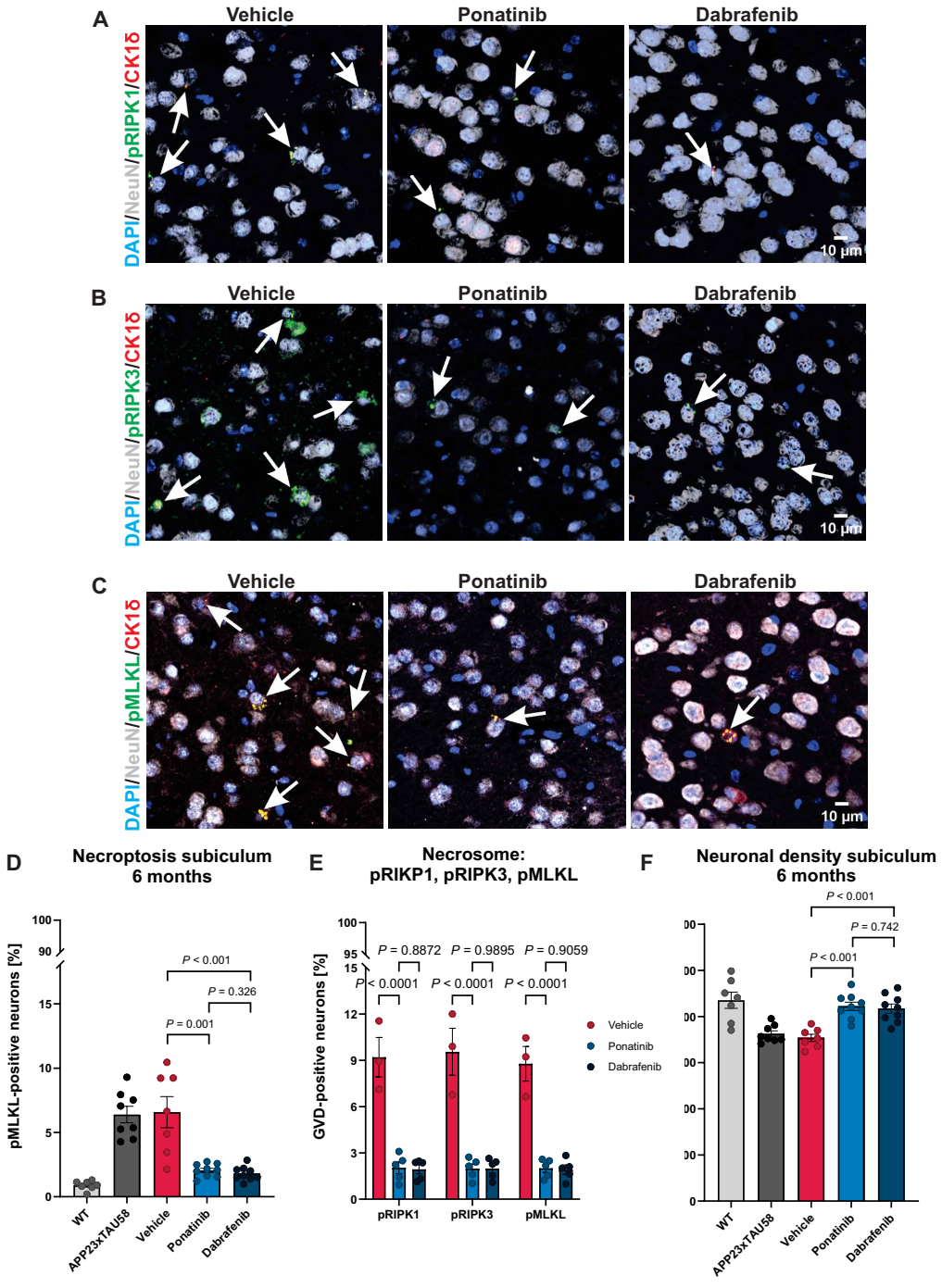

Fig. 6. Pharmacological inhibition of necroptosis reduces GVD-mediated necroptotic cell death in APP23xTAU58 mice. APP23xTAU58 mice between 2 and 6 months of age were administered ponatinib, dabrafenib, or vehicle for 16 weeks and then were euthanized, and their brains were fixed and stained for histopathology. Shown are representative immunofluorescence images stained for pRIPK1 [(**A**), green], pRIPK3 [(**B**), green] and pMLKL [(**C**), green], together with CK1δ (red), NeuN (gray), and DAPI (blue) in the subicula of 6-month-old APP23xTAU58 mice treated with vehicle, ponatinib, or dabrafenib. White arrows indicate subiculum neurons exhibiting necroptosis proteins. Single-channel images for the merged images in (A) to (C) are shown in fig. S6. (**D** to **F**) Quantification of the percentage of pMLKL-positive neurons relative to the total number of neurons (D) and the neuronal density (neurons per square millimeter) (F) in 6-month-old APP23xTAU58 animals is shown. The percentage of pMLKL-positive neurons and the neuronal density in WT littermates and untreated APP23xTAU58 mice are provided for comparison but were not used for statistical comparison. Quade ANCOVA was used to compare dabrafenib-treated and ponatinib-treated with vehicle-treated animals (see also table S7): WT, $n = 7$ animals; untreated APP23xTAU58 mice, $n = 8$; APP23xTAU58 mice treated with vehicle, $n = 7$; ponatinib, $n = 9$; or dabrafenib, $n = 9$. Data are presented as mean ± SEM. Post hoc power analysis indicated a power of ≥88.8% for comparisons among the three treatment groups. (E) Comparison of the percentage of GVD-positive neurons based on the presence of pRIPK1, pRIPK3, and pMLKL. Two-way ANOVA was performed showing uncorrected *P* values; *P* values corrected for multiple testing can be found in table S8; $P < 0.05$; vehicle, $n = 3$ animals; ponatinib, $n = 5$ mice; dabrafenib, $n = 5$ mice. Data are presented as mean ± SEM. Scale bars, 10 μm [(A) to (C)].

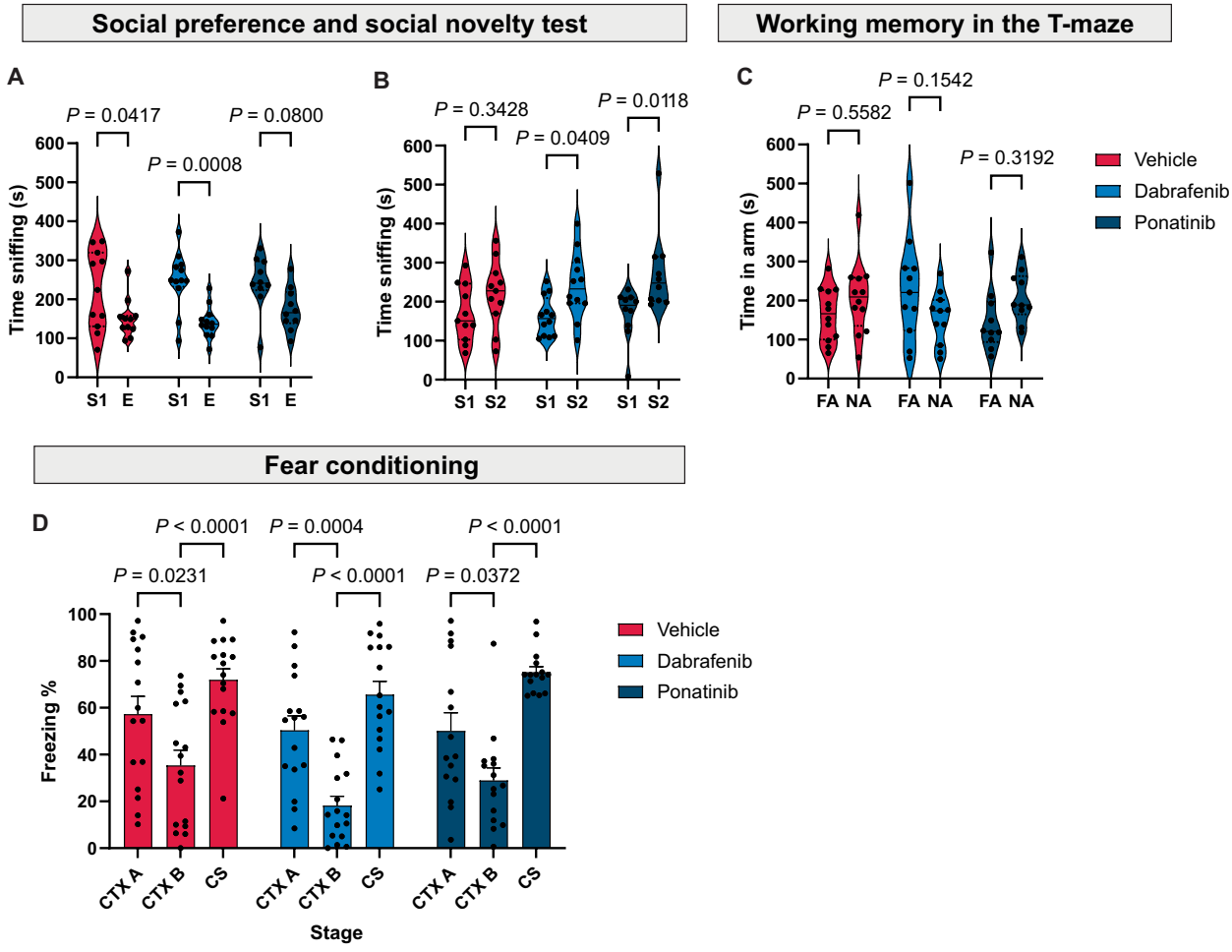

Fig. 7. Social recognition memory is improved after treatment with ponatinib or dabrafenib in APP23xTAU58 mice. Behavioral read-outs were performed at week 16 of the treatment period. (**A** and **B**) Shown are results of the social preference and social novelty behavior tests for dabrafenib-treated, ponatinib-treated, and vehicle-treated APP23xTAU58 mice. Sniffing time at stranger mouse 1 (S1) was compared with the empty chamber (E) and a novel stranger mouse 2 (S2). (**C**) Shown are results for the T-maze test for dabrafenib-, ponatinib-, and vehicle-treated APP23xTAU58 mice. Time spent in the familiar arm (FA) was compared with the novel arm (NA) during trial 2. In the first trial, the animals were allowed to explore the maze with the familiar arm while they had no access to the novel arm, which only opened in trial 2. (**D**) Freezing behavior was analyzed during a conditioned fear response experiment in APP23xTAU58 mice. Vehicle-treated, $n = 12$ animals; dabrafenib-treated, $n = 12$; ponatinib-treated, $n = 11$. Data are presented as mean ± SEM. Two-way ANOVA was performed, followed by Sidák's multiple comparisons test. CTX A, context A; CTX B, context B; CS, tone presentation plus interstimulus interval in context B.

recognition memory. Target engagement was demonstrated by the reduction of pRIPK1-positive, pRIPK3-positive, and pMLKL-positive neurons and an additional reduction of CK1δ-exhibiting GVD bodies. Our findings argue in favor of the relevance of GVD-necroptosis for neuronal death in the AD brain and are in line with previous reports showing necroptosis activation in AD (*11*, *12*, *18*). Given that this AD-associated form of necroptosis differs from "canonical necroptosis" by the accumulation of the necrosome in the vacuoles of GVD, we refer to it as "GVD-necroptosis" (*38*). The distinct morphological features of GVD-necroptosis in APP23xTAU58 mice compared with the previously reported necroptosis activation in mouse models of amyloidosis (*11*) point to the distinct nature of GVD-necroptosis occurring as a result of the combined AD pathology, for which Aβ pathology alone is not sufficient. The exacerbation of GVD-necroptosis in APP23xTAU58 mice compared with TAU58 or TAU22 mice could be explained by Aβ-accelerated tauopathy (*27*, *39*). Human stem cell–derived neurons transplanted into APP transgenic mice develop tau pathology and necrosome-positive GVD (*18*), supporting the hypothesis of an Aβ-accelerated tauopathy enabling GVD-necroptosis activation.

Considering that not all neurons with tau pathology accumulate pMLKL and GVD bodies, selective vulnerability might be relevant in these processes. Evidence from human AD supports the development of GVD-necroptosis in a subset of neurons in specific neuroanatomical regions (*12*). This hierarchical distribution pattern of GVD follows a similar pattern to pTau in humans (*17*) and transgenic mice, supporting the hypothesis that pTau is a major factor determining the vulnerability of neurons for developing GVD-necroptosis. In addition to pTau, neuronal subtype–specific functions, likely reflected by the proteome pattern (*37*), may explain why only some pTau-positive neurons develop GVD-necroptosis. In addition to GVD-necroptosis, NLR family pyrin domain containing 3 (NLRP3) inflammasome activation

and pyroptotic cell death contribute independently to hippocampal neuron loss in AD (*38*, *40*), indicating that GVD-necroptosis is not the only cell death pathway relevant in AD.

NLRP3 inflammasome and pyroptosis activation (*40*) and the release of cytokines, such as interleukin-1α (IL-1α), IL-1β, IL-6, IL-18, or tumor necrosis factor–α (TNFα), by microglial cells (*40*–*46*) possibly contribute to the activation of the necroptosis pathway (*47*). Specifically, GVD-necroptosis could represent TNFα-induced necroptosis modified by the endosomal system. ESCRT (endosomal sorting complexes required for transport) proteins colocalize with MLKL and the GVD marker Ck1δ (*48*, *49*) and mediate clearance of pMLKL from membranes via lysosomal degradation (*50*) and shedding of MLKL-damaged plasma membrane, contributing to cell survival (*51*). In addition, the release of pMLKL in exosomes has been shown to prevent cell death via necroptosis (*50*, *52*). Together with the reported role of pMLKL in enhancing endosomal transport (*52*), reduction of neuronal pMLKL could explain the observed decrease in GVD bodies after treatment with ponatinib and dabrafenib. Thus, insufficient release of pMLKL-containing vesicles, possibly reflected by the accumulation of GVD-necroptosis, could result in the formation of cytosolic pMLKL oligomers and their incorporation in the plasma membrane. Alternatively, disruption of the GVD vesicular membrane could lead to the incorporation of pMLKL oligomers into the cell membrane, or GVD bodies could fuse with the cell membrane. It requires further investigation to determine whether GVD represents a protective mechanism delaying necroptosis by storing the necroptosis proteins in GVD bodies and preventing pore formation in the cell membrane or whether pTau-triggered autophagic vacuoles (*36*) themselves serve as a place for unconventional RIPK1, RIPK3, and MLKL phosphorylation by, for example, casein kinases.

Ponatinib and dabrafenib were used to inhibit the necroptosis pathway in vivo, in line with previous work (*11*, *18*, *32*). Both drugs have been approved by the US Food and Drug Administration for use in humans with non-neurodegenerative conditions and inhibit RIPK1 and RIPK3 (*28*, *53*, *54*). However, the use of ponatinib and dabrafenib in preclinical/asymptomatic or early symptomatic patients with AD may be limited by possible adverse effects on the cardiovascular system (*29*), skin, and adrenal glands (*30*). Given that ponatinib and dabrafenib also inhibit kinases other than pRIPK1 and pRIPK3 (*28*), the specific effects of the inhibition of GVD-necroptosis were confirmed in vitro in primary mouse neurons treated with the RIPK1-specific inhibitor Nec-1s.

Our study has a number of limitations, including the restriction of pharmacological inhibition to mice aged between 2 and 6 months. At this time point, the animals did not develop evident amyloid aggregation or differences in synaptic density compared to WT animals. The effects of brain neuronal loss were presumably still being compensated for in these animals, possibly explaining the minor behavioral improvement after treatment, suggesting the benefit of cognitive reserve as has been found in human AD (*12*, *55*). Further, studies are necessary to investigate whether the inhibition of necroptosis can prevent neuronal loss and cognitive deficits in mice at later stages of AD pathology and with treatment starting after symptom onset at 6 months of age. The use of broad-spectrum kinase inhibitors for the inhibition of RIPK1 and RIPK3 is another limitation of our study. Although the targets differ, except for RIPK3, between dabrafenib [B-Raf proto-oncogene (BRAF), RAF-1 proto-oncogene (RAF1), salt-inducible kinase 1 (SIK1), NIMA-related kinase 11 (NEK11), and LIM-domain kinase 1 (LIMK1)] and ponatinib [BCR-ABL fusion oncoprotein, vascular endothelial growth factor receptor (VEGFR), platelet-derived growth factor receptor (PDGFR), fibroblast growth factor receptor (FGFR), ephrin receptor (EPHR), SRC proto-oncogene, KIT proto-oncogene, RET proto-oncogene, angiopoietin-1 receptor (TIE2), fms-like tyrosine kinase 3 (FLT3), transforming growth factor β–activated kinase 1 (TGF-β1), RIPK1, and RIPK2] (*28*), we cannot exclude the contribution of kinases other than RIPK1 and RIPK3 to neuronal loss in our mouse models or the anti-inflammatory effect described for dabrafenib (*56*). Future studies with specific inhibitors for RIPK1 and RIPK3 (*28*, *57*, *58*) should clarify whether necroptosis inhibition can protect mouse models of AD pathology from neuron death.

Collectively, our findings suggest that pTau aggregates may activate the GVD-necroptosis cell death pathway in mouse brain neurons. Inhibition of the GVD-necroptosis pathway using brain-penetrant small molecules targeting RIPK1 and RIPK3 reduced the activation of the necroptosis effector pMLKL and protected neurons from degeneration in mouse models of AD pathology. Contrary to canonical necroptosis, GVD-necroptosis presents a modified form of necroptosis that seems to delay neuronal death in AD mouse models. These findings indicate that necroptosis inhibition should be investigated further as a potential therapeutic strategy to complement Aβ and Tau-directed therapies for treating AD.

MATERIALS AND METHODS

Study design

The objective of this study was to investigate the role of necroptosis in AD-related neuronal loss. Specifically, the hypothesis to be tested was that inhibition of necroptosis leads to prevention of neuronal loss in a mouse model showing both Aβ and pTau pathologies. To do so, we first identified which mouse model of AD pathology was best suited for this purpose: APP23, TAU58, TAU22, or APP23x-TAU58 mice. For this purpose, histological brain samples were analyzed neuropathologically and immunohistochemically from the four mouse strains. On the basis of the respective findings, we carried out a controlled laboratory experiment using the cross-bred heterozygous APP23xTAU58 mouse model. Mice were assigned to three experimental groups using covariate adaptive randomization based on sex, littermates, and previously assigned treatment group: (i) vehicle [5% dimethyl sulfoxide + 50% polyethylene glycol (PEG) 300 (v/v) in distilled water]; (ii) ponatinib (ponatinib; 10 mg/kg); or (iii) dabrafenib (dabrafenib; 30 mg/kg). Confounders regarding the treatment protocol were not specifically controlled for. Animals from 2 to 6 months old were treated for 16 weeks. Drugs were administered via intraperitoneal injection during 5 weekdays, followed by a 2-day rest. Under normal circumstances, 6-month-old mice were subjected to behavioral analyses (contextual and cued fear conditioning, social preference and social novelty test, and working memory in the T-maze), followed by euthanasia. The right brain hemispheres were then collected to create formalin-fixed paraffin-embedded tissue sections for immunohistochemical staining. These were used to assess the neuronal density, the amount of neurons positive for necroptosis-related proteins, pTau load and distribution, the presence and phase of Aβ pathology, and synaptic density. The primary outcome measure was the neuronal density as a measure for neuronal loss. The researchers conducting the behavioral experiments and histopathological quantifications were blinded to the experimental conditions. At the stage of data analysis, data points were assigned to their respective experimental groups. The experiment was stopped

for animals reaching the following intermediary end points: (i) getting a severe infection, (ii) weight loss of 20% in 1 week, (iii) developing severe neurological or motor symptoms, and (iv) developing chronic wounds. These points were checked during 5 weekdays. Mice reaching these intermediary end points were euthanized and not included in the study. No outliers were identified or excluded from the study. To keep the number of mice to a minimum, in line with the ethical guidelines for mouse experiments, the experiment was not replicated. Analyses were performed using biological replicates. The study protocol was prepared and provided to the Ethical Committee for approval but not specifically registered before starting the study. The animal experiments were carried out according to ARRIVE (Animal Research: Reporting of In Vivo Experiments) guidelines. Experiments in cultured mouse primary neurons were used to support the mouse experiments in an in vitro approach. Additional information on the drug treatment and the behavioral tests is provided in Supplementary Materials and Methods.

Animals

Heterozygous transgenic (APP23, TAU58, TAU22, and APP23xTAU58) mice of both sexes were included in the study. Nontransgenic littermates (WT) on a C57BL/6J background were used as controls. Table S1 summarizes the information regarding each mouse strain used in the study. The APP23 transgenic model harbors the Swedish double mutation (K670M/N671L) in APP under the control of the neuron-specific murine Thy-1 promoter and develops Aβ deposits in the neocortex at the age of 6 months (*20*). TAU58 mice express the human 04NR tau isoform with a neuronal P301S mutation under the Thy1.2 murine promoter and present tau pathology in the brainstem already at the age of 3 months (*21*). The TAU22 transgenic line is a well-characterized model of tauopathy that was generated by combining G272V and P301S mutations on the four-repeat isoform of human tau under the control of the Thy1.2 promoter (*22*). The double-transgenic APP23xTAU58 mouse model of both Aβ and tau pathologies was used to more closely mimic human AD neuropathology. To generate APP23xTAU58 mice, TAU58 mice were crossed with APP23 mice (APP23xTAU58) (*27*). Female tau and male APP mice were housed together without separation for a maximum of four nests or 9 months of age. Animals were housed in groups under conventional laboratory conditions (14-hour light/10-hour dark cycle; 22° ± 2°C; humidity, 45 to 70%) with free access to food and water. Filter-top cages were enriched with two cotton pellets replaced during cage changing. Animal experiments were conducted according to protocols approved by the local Ethical Committee of Laboratory Animals (ECD) of the Katholieke Universiteit Leuven (KU Leuven) (ECD project number P191-2020). Breeding of APP23, TAU58, and APP23xTAU58 mice for neuropathological analysis was partially carried out at the Novartis Institutes of Biomedical Research according to Swiss law (permission nos: BS-1795, BW-1094, and BW-444). TAU22 mice were bred exclusively in Leuven according to Belgian law. All efforts were made to treat the mice humanely, follow ethical guidelines, and use only the number of animals needed to generate reliable scientific data.

Immunohistology

After a 16-week treatment period, mice were anesthetized with a ketamine and medetomidine mixture (75 and 1 mg/kg, intraperitoneally). After cardiac perfusion with 10 ml of 5% heparin solution in precooled sterile Dulbecco's phosphate-buffered saline (PBS; Gibco), brains were collected. Livers and right brain hemispheres, including brainstems and cerebellums, were fixed for 24 hours in paraformaldehyde (PFA) before being transferred to PBS and stored at 4°C for further tissue processing. The left brain hemisphere was kept snap frozen. Dehydrated and paraffin-embedded tissues were cut into 5-μm-thick consecutive sections (the sagittal plane was used for brain samples).

For immunohistochemistry and immunofluorescence (IF) staining, we followed the protocols that our group previously reported (*12*). Briefly, sections were deparaffinized, rehydrated, and incubated with mouse immunoglobulin G block for 30 min at room temperature. Pretreatment was carried out depending on the respective primary antibodies (table S4). After the overnight incubation with primary antibodies at room temperature, the sections were washed and probed with corresponding secondary antibodies. Immunoreactivity of the protein of interest was visualized with 3,3′-diaminobenzidine (DAB) substrate (liquid DAB + Substrate Chromogen System, Dako), and hematoxylin was used to counterstain the nuclei. IF stainings were performed with two- or three-antibody cocktails. Nuclear staining was performed using Hoechst 33342 solution (Thermo Fisher Scientific). Table S2 summarizes the information regarding each antibody used in the study. Light and fluorescence microscopy (DM2000 light-emitting diode microscope + DFC7000 T camera, Leica Microsystems) was used to analyze DAB and IF immunostaining, whereas fluorescent microscopic observations were also carried out using a Nikon A1R laser scanning confocal system coupled to a Nikon Eclipse Ti inverted microscope (Nikon Instruments Inc.). For quantitative analyses, z-stack scans of a large area of the brain sections, covering the affected regions by GVD-necroptosis, were acquired. To create 3D reconstructions of positive neurons, z-stack confocal images of multiple labeled sections were processed using Imaris software (Bitplane). Details on image processing; quantitative analyses; and the determination of the distribution patterns of GVD-necroptosis, Aβ plaques, and pTau pathology can be found in Supplementary Materials and Methods.

Treatment of primary hippocampal and cortical cultures with tau seeds

Primary mouse cortical and hippocampal cultures were derived from pregnant double transgenic mice ($App^{NL\text{-}G\text{-}F}$; $Tau22^{tg/wt}$) at embryonic day 17. The cells were seeded at 10,000 to 15,000 cells/cm^2. On the in vitro day 5, Si-AD tau treatments were done in the neurobasal with B27+ medium at a concentration of 1.5 μg/ml. The Si-AD tau seeds were sonicated (20 pulses at 1 s per pulse, 60% amplitude) using a water bath sonicator (QSonica) and added to the medium at a concentration of approximately 1.5 μg/ml. Stimulation with tau seeds was done only once, and 50% of the medium was replenished with glia-conditioned medium every 4 to 5 days. Necroptosis inhibitor, Nec-1s, was used at a concentration of 0.5 μM, starting from day 5 of tau stimulation until the end of the experiment. CellTiter-Glo luminescent cell viability assay and IF analysis were performed. Additional information on the primary hippocampal and cortical neuron cultures and the CellTiter-Glo assay is provided in Supplementary Materials and Methods.

In vitro IF and confocal imaging

For the IF analysis, cells were washed three times with PBS and fixed either with ice-cold methanol (−80°C stored) for 15 min on ice or with 4% PFA for 15 min at room temperature. After fixation, cells were washed three times with tris-buffered saline with Tween (TBST) containing 0.3% Triton X-100. Subsequently, blocking buffer (0.3%

Triton X-100 in TBST, 2% BSA, and 3% donkey serum) was added to cells at room temperature for 1 hour. The primary antibody (see table S4), diluted in the blocking buffer, was added to the cells and incubated overnight at 4°C with gentle rotation. The following day, cells were washed with TBST, and respective secondary antibodies were added to the cells and incubated for 2 hours at room temperature. After 2 hours, cells were washed with TBST three times. Approximately 30 μl of Glycergel mounting medium was added to the wells before imaging. Confocal images with z-stacks were obtained using a Nikon Ti-E invert microscope equipped with an A1R confocal unit driven by Nikon imaging software (NIS version 4.30). For excitation, 405-, 488-, 561-, and 638-nm laser lines were used. For image processing, the Fiji/ImageJ software was used. The methodology used for the isolation of sarkosyl-insoluble tau from a human postmortem AD brain, in vitro culture conditions, and details on the CellTiter-Glo luminescent cell viability assay can be found in Supplementary Materials and Methods.

Statistical analysis

The data were analyzed with unpaired two-tailed sample *t* tests or repeated measures ANOVA using a one-way or two-way ANOVA. Reported *P* values are uncorrected, supplemented by multiple testing correction as reported in figure legends or supplementary tables. Normality was assessed with the Shapiro-Wilks test, and when violated, nonparametric statistics were applied (Mann-Whitney or Kruskal-Wallis). Survival analysis was performed using Kaplan-Meier followed by the log-rank (Mantel-Cox) test. To control for differences in sex distribution, we used analysis of covariance (ANCOVA) comparing the dabrafenib- and ponatinib-treated groups with the vehicle-treated animals controlled for sex. Binary logistic regression analysis was used to determine target engagement in the treated animals (separately for dabrafenib- and ponatinib-treated mice) in a model containing the distribution of GVD-necroptosis (pMLKL-positive brain regions), pTau distribution (number of brain regions with pTau pathology), and Aβ phase in APP transgenic mice according to Thal *et al.* (*25*). Post hoc power analysis was carried out for comparisons of the neuronal densities and frequencies of GVD-necroptosis–affected neurons among the different mouse models at 12 months of age and among the treatment groups. All bars and error bars represent the mean values ± SEM. All analyses were performed using SPSS v.22 (SPSS Inc.) and GraphPad Prism 9 software (GraphPad Software Inc.). The significance was set at $P < 0.05$. Descriptive statistics including mean and SEM and normal quantile-quantile (QQ) plots are provided in data file S3.

Supplementary Materials

The PDF file includes:
Materials and Methods
Figs. S1 to S10
Tables S1 to S10
References (*59*–*72*)

Other Supplementary Material for this manuscript includes the following:
Data files S1 to S3
MDAR Reproducibility Checklist

REFERENCES AND NOTES

1. Alzheimer's Association, 2023 Alzheimer's disease facts and figures. *Alzheimers Dement.* **19**, 1598–1695 (2023).
2. I. Grundke-Iqbal, K. Iqbal, Y. C. Tung, M. Quinlan, H. M. Wisniewski, L. I. Binder, Abnormal phosphorylation of the microtubule-associated protein tau (tau) in Alzheimer cytoskeletal pathology. *Proc. Natl. Acad. Sci. U.S.A.* **83**, 4913–4917 (1986).
3. C. L. Masters, G. Simms, N. A. Weinman, G. Multhaup, B. L. McDonald, K. Beyreuther, Amyloid plaque core protein in Alzheimer disease and Down syndrome. *Proc. Natl. Acad. Sci. U.S.A.* **82**, 4245–4249 (1985).
4. J. Cummings, Y. Zhou, G. Lee, K. Zhong, J. Fonseca, F. Cheng, Alzheimer's disease drug development pipeline: 2023. *Alzheimers Dement.* **9**, e12385 (2023).
5. K. Y. Liu, R. Howard, Can we learn lessons from the FDA's approval of aducanumab? *Nat. Rev. Neurol.* **17**, 715–722 (2021).
6. E. Teng, P. T. Manser, K. Pickthorn, F. Brunstein, M. Blendstrup, S. Sanabria Bohorquez, K. R. Wildsmith, B. Toth, M. Dolton, V. Ramakrishnan, A. Bobbala, S. A. M. Sikkes, M. Ward, R. N. Fuji, G. A. Kerchner; Tauriel Investigators, Safety and efficacy of semorinemab in individuals with prodromal to mild Alzheimer disease: A randomized clinical trial. *JAMA Neurol.* **79**, 758–767 (2022).
7. J. R. Sims, J. A. Zimmer, C. D. Evans, M. Lu, P. Ardayfio, J. Sparks, A. M. Wessels, S. Shcherbinin, H. Wang, E. S. Monkul Nery, E. C. Collins, P. Solomon, S. Salloway, L. G. Apostolova, O. Hansson, C. Ritchie, D. A. Brooks, M. Mintun, D. M. Skovronsky, T.-A. Investigators, Donanemab in early symptomatic Alzheimer disease: The TRAILBLAZER-ALZ 2 randomized clinical trial. *JAMA* **330**, 512–527 (2023).
8. J. A. Nicoll, D. Wilkinson, C. Holmes, P. Steart, H. Markham, R. O. Weller, Neuropathology of human Alzheimer disease after immunization with amyloid-beta peptide: A case report. *Nat. Med.* **9**, 448–452 (2003).
9. E. D. Plowey, T. Bussiere, R. Rajagovindan, J. Sebalusky, S. Hamann, C. von Hehn, C. Castrillo-Viguera, A. Sandrock, S. Budd Haeberlein, C. H. van Dyck, A. Huttner, Alzheimer disease neuropathology in a patient previously treated with aducanumab. *Acta Neuropathol.* **144**, 143–153 (2022).
10. L. Sun, H. Wang, Z. Wang, S. He, S. Chen, D. Liao, L. Wang, J. Yan, W. Liu, X. Lei, X. Wang, Mixed lineage kinase domain-like protein mediates necrosis signaling downstream of RIP3 kinase. *Cell* **148**, 213–227 (2012).
11. A. Caccamo, C. Branca, I. S. Piras, E. Ferreira, M. J. Huentelman, W. S. Liang, B. Readhead, J. T. Dudley, E. E. Spangenberg, K. N. Green, R. Belfiore, W. Winslow, S. Oddo, Necroptosis activation in Alzheimer's disease. *Nat. Neurosci.* **20**, 1236–1246 (2017).
12. M. J. Koper, E. Van Schoor, S. Ospitalieri, R. Vandenberghe, M. Vandenbulcke, C. A. F. von Arnim, T. Tousseyn, S. Balusu, B. De Strooper, D. R. Thal, Necrosome complex detected in granulovacuolar degeneration is associated with neuronal loss in Alzheimer's disease. *Acta Neuropathol.* **139**, 463–484 (2020).
13. Z. Cai, S. Jitkaew, J. Zhao, H. C. Chiang, S. Choksi, J. Liu, Y. Ward, L. G. Wu, Z. G. Liu, Plasma membrane translocation of trimerized MLKL protein is required for TNF-induced necroptosis. *Nat. Cell. Biol.* **16**, 55–65 (2014).
14. U. Ros, A. Pena-Blanco, K. Hanggi, U. Kunzendorf, S. Krautwald, W. W. Wong, A. J. Garcia-Saez, Necroptosis execution is mediated by plasma membrane nanopores independent of calcium. *Cell Rep.* **19**, 175–187 (2017).
15. M. J. Ball, P. Lo, Granulovacuolar degeneration in the ageing brain and in dementia. *J. Neuropathol. Exp. Neurol.* **36**, 474–487 (1977).
16. T. Simchowicz, in *Histologie und histopathologische Arbeiten über die Großhirnrinde*, F. Nissl, A. Alzheimer, Eds. (Fischer, 1911), vol. 4, pp. 267–444.
17. D. R. Thal, K. Del Tredici, A. C. Ludolph, J. J. Hoozemans, A. J. Rozemuller, H. Braak, U. Knippschild, Stages of granulovacuolar degeneration: Their relation to Alzheimer's disease and chronic stress response. *Acta Neuropathol.* **122**, 577–589 (2011).
18. S. Balusu, K. Horre, N. Thrupp, K. Craessaerts, A. Snellinx, L. Serneels, D. T'Syen, I. Chrysidou, A. M. Arranz, A. Sierksma, J. Simren, T. K. Karikari, H. Zetterberg, W. T. Chen, D. R. Thal, E. Salta, M. Fiers, B. De Strooper, MEG3 activates necroptosis in human neuron xenografts modeling Alzheimer's disease. *Science* **381**, 1176–1182 (2023).
19. C. Köhler, M. Dinekov, J. Götz, Granulovacuolar degeneration and unfolded protein response in mouse models of tauopathy and Abeta amyloidosis. *Neurobiol. Dis.* **71**, 169–179 (2014).
20. C. Sturchler-Pierrat, D. Abramowski, M. Duke, K. H. Wiederhold, C. Mistl, S. Rothacher, B. Ledermann, K. Burki, P. Frey, P. A. Paganetti, C. Waridel, M. E. Calhoun, M. Jucker, A. Probst, M. Staufenbiel, B. Sommer, Two amyloid precursor protein transgenic mouse models with Alzheimer disease-like pathology. *Proc. Natl. Acad. Sci. U.S.A.* **94**, 13287–13292 (1997).
21. J. van Eersel, C. H. Stevens, M. Przybyla, A. Gladbach, K. Stefanoska, C. K. Chan, W. Y. Ong, J. R. Hodges, G. T. Sutherland, J. J. Kril, D. Abramowski, M. Staufenbiel, G. M. Halliday, L. M. Ittner, Early-onset axonal pathology in a novel P301S-Tau transgenic mouse model of frontotemporal lobar degeneration. *Neuropathol. Appl. Neurobiol.* **41**, 906–925 (2015).
22. K. Schindowski, A. Bretteville, K. Leroy, S. Begard, J. P. Brion, M. Hamdane, L. Buee, Alzheimer's disease-like tau neuropathology leads to memory deficits and loss of functional synapses in a novel mutated tau transgenic mouse without any motor deficits. *Am. J. Pathol.* **169**, 599–616 (2006).

23. L. A. Gomes, V. Uytterhoeven, D. Lopez-Sanmartin, S. O. Tome, T. Tousseyn, R. Vandenberghe, M. Vandenbulcke, C. A. F. von Arnim, P. Verstreken, D. R. Thal, Maturation of neuronal AD-tau pathology involves site-specific phosphorylation of cytoplasmic and synaptic tau preceding conformational change and fibril formation. *Acta Neuropathol.* **141**, 173–192 (2021).
24. C. Schwab, A. J. DeMaggio, N. Ghoshal, L. I. Binder, J. Kuret, P. L. McGeer, Casein kinase 1 delta is associated with pathological accumulation of tau in several neurodegenerative diseases. *Neurobiol. Aging* **21**, 503–510 (2000).
25. D. R. Thal, E. Capetillo-Zarate, K. Del Tredici, H. Braak, The development of amyloid beta protein deposits in the aged brain. *Sci. Aging Knowledge Environ.* **2006**, re1 (2006).
26. S. Jeganathan, A. Hascher, S. Chinnathambi, J. Biernat, E. M. Mandelkow, E. Mandelkow, Proline-directed pseudo-phosphorylation at AT8 and PHF1 epitopes induces a compaction of the paperclip folding of Tau and generates a pathological (MC-1) conformation. *J. Biol. Chem.* **283**, 32066–32076 (2008).
27. L. A. Gomes, S. A. Hipp, A. Rijal Upadhaya, K. Balakrishnan, S. Ospitalieri, M. J. Koper, P. Largo-Barrientos, V. Uytterhoeven, J. Reichwald, S. Rabe, R. Vandenberghe, C. A. F. von Arnim, T. Tousseyn, R. Feederle, C. Giudici, M. Willem, M. Staufenbiel, D. R. Thal, Aβ-induced acceleration of Alzheimer-related tau-pathology spreading and its association with prion protein. *Acta Neuropathol.* **138**, 913–941 (2019).
28. S. Martens, S. Hofmans, W. Declercq, K. Augustyns, P. Vandenabeele, Inhibitors targeting RIPK1/RIPK3: Old and new drugs. *Trends Pharmacol. Sci.* **41**, 209–224 (2020).
29. O. Chan, C. Talati, L. Isenalumhe, S. Shams, L. Nodzon, M. Fradley, K. Sweet, J. Pinilla-Ibarz, Side-effects profile and outcomes of ponatinib in the treatment of chronic myeloid leukemia. *Blood Adv.* **4**, 530–538 (2020).
30. M. Schreuer, Y. Jansen, S. Planken, I. Chevolet, T. Seremet, V. Kruse, B. Neyns, Combination of dabrafenib plus trametinib for BRAF and MEK inhibitor pretreated patients with advanced $BRAF^{V600}$-mutant melanoma: An open-label, single arm, dual-centre, phase 2 clinical trial. *Lancet Oncol.* **18**, 464–472 (2017).
31. A. Puszkiel, G. Noé, A. Bellesoeur, N. Kramkimel, M.-N. Paludetto, A. Thomas-Schoemann, M. Vidal, F. Goldwasser, E. Chatelut, B. Blanchet, Clinical pharmacokinetics and pharmacodynamics of dabrafenib. *Clin. Pharmacokinet.* **58**, 451–467 (2018).
32. Y. Dong, H. Yu, X. Li, K. Bian, Y. Zheng, M. Dai, X. Feng, Y. Sun, Y. He, B. Yu, H. Zhang, J. Wu, X. Yu, H. Wu, W. Kong, Hyperphosphorylated tau mediates neuronal death by inducing necroptosis and inflammation in Alzheimer's disease. *J. Neuroinflammation* **19**, 205 (2022).
33. S. Balusu, B. De Strooper, The necroptosis cell death pathway drives neurodegeneration in Alzheimer's disease. *Acta Neuropathol.* **147**, 96 (2024).
34. H. Braak, E. Braak, Neuropathological stageing of Alzheimer-related changes. *Acta Neuropathol.* **82**, 239–259 (1991).
35. D. E. Hurtado, L. Molina-Porcel, M. Iba, A. K. Aboagye, S. M. Paul, J. Q. Trojanowski, V. M. Lee, Aβ accelerates the spatiotemporal progression of Tau pathology and augments Tau amyloidosis in an Alzheimer mouse model. *Am. J. Pathol.* **177**, 1977–1988 (2010).
36. V. I. Wiersma, A. M. van Ziel, S. Vazquez-Sanchez, A. Nolle, E. Berenjeno-Correa, A. Bonaterra-Pastra, F. Clavaguera, M. Tolnay, R. J. P. Musters, J. R. T. van Weering, M. Verhage, J. J. M. Hoozemans, W. Scheper, Granulovacuolar degeneration bodies are neuron-selective lysosomal structures induced by intracellular tau pathology. *Acta Neuropathol.* **138**, 943–970 (2019).
37. D. C. Hondius, F. Koopmans, C. Leistner, D. Pita-Illobre, R. M. Peferoen-Baert, F. Marbus, I. Paliukhovich, K. W. Li, A. J. M. Rozemuller, J. J. M. Hoozemans, A. B. Smit, The proteome of granulovacuolar degeneration and neurofibrillary tangles in Alzheimer's disease. *Acta Neuropathol.* **141**, 341–358 (2021).
38. D. R. Thal, K. Gawor, S. Moonen, Regulated cell death and its role in Alzheimer's disease and amyotrophic lateral sclerosis. *Acta Neuropathol.* **147**, 69 (2024).
39. G. T. Corbett, Z. Wang, W. Hong, M. Colom-Cadena, J. Rose, M. Liao, A. Asfaw, T. C. Hall, L. Ding, A. DeSousa, M. P. Frosch, J. Collinge, D. A. Harris, M. S. Perkinton, T. L. Spires-Jones, T. L. Young-Pearse, A. Billinton, D. M. Walsh, PrP is a central player in toxicity mediated by soluble aggregates of neurodegeneration-causing proteins. *Acta Neuropathol.* **139**, 503–526 (2020).
40. S. Moonen, M. J. Koper, E. Van Schoor, J. M. Schaeverbeke, R. Vandenberghe, C. A. F. von Arnim, T. Tousseyn, B. De Strooper, D. R. Thal, Pyroptosis in Alzheimer's disease: Cell type-specific activation in microglia, astrocytes and neurons. *Acta Neuropathol.* **145**, 175–195 (2023).
41. W. S. Griffin, J. G. Sheng, G. W. Roberts, R. E. Mrak, Interleukin-1 expression in different plaque types in Alzheimer's disease: Significance in plaque evolution. *J. Neuropathol. Exp. Neurol.* **54**, 276–281 (1995).
42. W. S. Griffin, L. C. Stanley, C. Ling, L. White, V. MacLeod, L. J. Perrot, C. L. White III, C. Araoz, Brain interleukin 1 and S-100 immunoreactivity are elevated in Down syndrome and Alzheimer disease. *Proc. Natl. Acad. Sci. U.S.A.* **86**, 7611–7615 (1989).
43. J. G. Sheng, R. E. Mrak, W. S. Griffin, Glial-neuronal interactions in Alzheimer disease: Progressive association of IL-1α^{+} microglia and S100β^{+} astrocytes with neurofibrillary tangle stages. *J. Neuropathol. Exp. Neurol.* **56**, 285–290 (1997).
44. S. Strauss, J. Bauer, U. Ganter, U. Jonas, M. Berger, B. Volk, Detection of interleukin-6 and alpha 2-macroglobulin immunoreactivity in cortex and hippocampus of Alzheimer's disease patients. *Lab. Invest* **66**, 223–230 (1992).
45. A. D. Greenhalgh, S. David, F. C. Bennett, Immune cell regulation of glia during CNS injury and disease. *Nat. Rev. Neurosci.* **21**, 139–152 (2020).
46. J. S. Ha, H. R. Choi, I. S. Kim, E. A. Kim, S. W. Cho, S. J. Yang, Hypoxia-induced S100A8 expression activates microglial inflammation and promotes neuronal apoptosis. *Int. J. Mol. Sci.* **22**, 1205 (2021).
47. D. Tang, R. Kang, T. V. Berghe, P. Vandenabeele, G. Kroemer, The molecular machinery of regulated cell death. *Cell Res.* **29**, 347–364 (2019).
48. K. E. Funk, R. E. Mrak, J. Kuret, Granulovacuolar degeneration bodies of Alzheimer's disease resemble late-stage autophagic organelles. *Neuropathol. Appl. Neurobiol.* **37**, 295–306 (2011).
49. A. Jayaraman, T. T. Htike, R. James, C. Picon, R. Reynolds, TNF-mediated neuroinflammation is linked to neuronal necroptosis in Alzheimer's disease hippocampus. *Acta Neuropathol. Commun.* **9**, 159 (2021).
50. W. Fan, J. Guo, B. Gao, W. Zhang, L. Ling, T. Xu, C. Pan, L. Li, S. Chen, H. Wang, J. Zhang, X. Wang, Flotillin-mediated endocytosis and ALIX-syntenin-1-mediated exocytosis protect the cell membrane from damage caused by necroptosis. *Sci. Signal.* **12**, eaaw3423 (2019).
51. Y. N. Gong, C. Guy, H. Olauson, J. U. Becker, M. Yang, P. Fitzgerald, A. Linkermann, D. R. Green, ESCRT-III acts downstream of MLKL to regulate necroptotic cell death and its consequences. *Cell* **169**, 286–300.e16 (2017).
52. S. Yoon, A. Kovalenko, K. Bogdanov, D. Wallach, MLKL, the protein that mediates necroptosis, also regulates endosomal trafficking and extracellular vesicle generation. *Immunity* **47**, 51–65.e7 (2017).
53. M. Najjar, C. Suebsuwong, S. S. Ray, R. J. Thapa, J. L. Maki, S. Nogusa, S. Shah, D. Saleh, P. J. Gough, J. Bertin, J. Yuan, S. Balachandran, G. D. Cuny, A. Degterev, Structure guided design of potent and selective ponatinib-based hybrid inhibitors for RIPK1. *Cell Rep.* **10**, 1850–1860 (2015).
54. S. A. Cruz, Z. Qin, A. F. R. Stewart, H. H. Chen, Dabrafenib, an inhibitor of RIP3 kinase-dependent necroptosis, reduces ischemic brain injury. *Neural Regen. Res.* **13**, 252–256 (2018).
55. M. J. West, Regionally specific loss of neurons in the aging human hippocampus. *Neurobiol. Aging* **14**, 287–293 (1993).
56. S. Lee, S.-K. Ku, J.-S. Bae, Anti-inflammatory effects of dabrafenib on polyphosphate-mediated vascular disruption. *Chem. Biol. Interact.* **256**, 266–273 (2016).
57. A. Hincelin-Mery, X. Nicolas, C. Cantalloube, R. Pomponio, P. Lewanczyk, M. Benamor, D. Ofengeim, E. Krupka, J. Hsiao-Nakamoto, A. Eastenson, N. Atassi, Safety, pharmacokinetics, and target engagement of a brain penetrant RIPK1 inhibitor, SAR443820 (DNL788), in healthy adult participants. *Clin. Transl. Sci.* **17**, e13690 (2024).
58. M. Liu, H. Li, R. Yang, D. Ji, X. Xia, GSK872 and necrostatin-1 protect retinal ganglion cells against necroptosis through inhibition of RIP1/RIP3/MLKL pathway in glutamate-induced retinal excitotoxic model of glaucoma. *J. Neuroinflammation* **19**, 262 (2022).
59. A. Fauster, M. Rebsamen, K. V. Huber, J. W. Bigenzahn, A. Stukalov, C. H. Lardeau, S. Scorzoni, M. Bruckner, M. Gridling, K. Parapatics, J. Colinge, K. L. Bennett, S. Kubicek, S. Krautwald, A. Linkermann, G. Superti-Furga, A cellular screen identifies ponatinib and pazopanib as inhibitors of necroptosis. *Cell Death Dis.* **6**, e1767 (2015).
60. J. X. Li, J. M. Feng, Y. Wang, X. H. Li, X. X. Chen, Y. Su, Y. Y. Shen, Y. Chen, B. Xiong, C. H. Yang, J. Ding, Z. H. Miao, The $B\text{-}Raf^{V600E}$ inhibitor dabrafenib selectively inhibits RIP3 and alleviates acetaminophen-induced liver injury. *Cell Death Dis.* **5**, e1278 (2014).
61. L. Trovò, T. Ahmed, Z. Callaerts-Vegh, A. Buzzi, C. Bagni, M. Chuah, T. Vandendriessche, R. D'Hooge, D. Balschun, C. G. Dotti, Low hippocampal $PI(4,5)P_2$ contributes to reduced cognition in old mice as a result of loss of MARCKS. *Nat. Neurosci.* **16**, 449–455 (2013).
62. Allen Institute for Brain Science (2011); mouse.brain-map.org.
63. M. E. Murray, N. R. Graff-Radford, O. A. Ross, R. C. Petersen, R. Duara, D. W. Dickson, Neuropathologically defined subtypes of Alzheimer's disease with distinct clinical characteristics: A retrospective study. *Lancet Neurol.* **10**, 785–796 (2011).
64. J. L. Guo, S. Narasimhan, L. Changolkar, Z. He, A. Stieber, B. Zhang, R. J. Gathagan, M. Iba, J. D. McBride, J. Q. Trojanowski, V. M. Y. Lee, Unique pathological tau conformers from Alzheimer's brains transmit tau pathology in nontransgenic mice. *J. Exp. Med.* **213**, 2635–2654 (2016).
65. V. I. Wiersma, W. Scheper, Granulovacuolar degeneration bodies: Red alert for neurons with MAPT/tau pathology. *Autophagy* **16**, 173–175 (2019).
66. D. R. Thal, E. Ghebremedhin, C. Haass, C. Schultz, UV light-induced autofluorescence of full-length Abeta-protein deposits in the human brain. *Clin. Neuropathol.* **21**, 35–40 (2002).
67. C. Sauvey, G. Ehrenkaufer, D. Shi, A. Debnath, R. Abagyan, Antineoplastic kinase inhibitors: A new class of potent anti-amoebic compounds. *PLOS Negl. Trop. Dis.* **15**, e0008425 (2021).
68. A. J. King, M. R. Arnone, M. R. Bleam, K. G. Moss, J. Yang, K. E. Fedorowicz, K. N. Smitheman, J. A. Erhardt, A. Hughes-Earle, L. S. Kane-Carson, R. H. Sinnamon, H. Qi, T. R. Rheault,

D. E. Uehling, S. G. Laquerre, Dabrafenib; preclinical characterization, increased efficacy when combined with trametinib, while BRAF/MEK tool combination reduced skin lesions. *PLOS ONE* **8**, e67583 (2013).
69. I. C. Waizenegger, A. Baum, S. Steurer, H. Stadtmuller, G. Bader, O. Schaaf, P. Garin-Chesa, A. Schlattl, N. Schweifer, C. Haslinger, F. Colbatzky, S. Mousa, A. Kalkuhl, N. Kraut, G. R. Adolf, A novel RAF kinase inhibitor with DFG-out-binding mode: High efficacy in BRAF-mutant tumor xenograft models in the absence of normal tissue hyperproliferation. *Mol. Cancer Ther.* **15**, 354–365 (2016).
70. K. Ravi, A. Franson, M. J. Homan, H. Roberts, M. P. Pai, Z. Miklja, M. He, B. Wen, L. L. Benitez, A. J. Perissinotti, D. L. Bixby, C. Koschmann, B. L. Marini, Comparative pharmacokinetic analysis of the blood-brain barrier penetration of dasatinib and ponatinib in mice. *Leuk. Lymphoma* **62**, 1990–1994 (2021).
71. R. K. Mittapalli, S. Vaidhyanathan, A. Z. Dudek, W. F. Elmquist, Mechanisms limiting distribution of the threonine-protein kinase B-Raf^{V600E} inhibitor dabrafenib to the brain: Implications for the treatment of melanoma brain metastases. *J. Pharmacol. Exp. Ther.* **344**, 655–664 (2013).
72. T. Sugaya, H. Kanno, M. Matsuda, K. Handa, S. Tateda, T. Murakami, H. Ozawa, E. Itoi, B-RAF^{V600E} inhibitor dabrafenib attenuates RIPK3-mediated necroptosis and promotes functional recovery after spinal cord injury. *Cells* **8**, 1582 (2019).

Acknowledgments: We thank the VIB Imaging Core Facility in Leuven for expert assistance and overall technical support in imaging analysis. Also, we thank our colleagues from the Animal Facility at KU Leuven for taking care of our animals. We thank the late P. Davies, Department of Pathology, Albert Einstein College of Medicine for the gift of the MC1 antibody. We thank K. Horré, A. Snellinx, and K. Craessaerts for expert help with tissue cultures. **Funding:** This work was supported by Fonds Wetenschappelijk Onderzoek (FWO, Belgium) G0F8516N (D.R.T.) and 12P5922N (S.B. and B.D.S.), Flemish Government and the KU Leuven internal funds (Belgium) Methusalem grant 3M140280 (B.D.S.), European Research Council (ERC) under the European Union's Horizon 2020 Research and Innovation Programme (grant agreement no. 834682), KU-Leuven Internal Funds C14/22/132 (D.R.T.), Stichting Alzheimer Onderzoek (SAO-FRA, Belgium) 2023/0009 (D.R.T.) and 2022/023 (B.D.S.), Queen Elisabeth Medical Foundation for Neurosciences (UK) ZKE3683 (B.D.S.), GSKE Ernest Solvay Prize (UK) ENA-E5665-GSKE (S.B.), and The Opening the Future campaign of the Leuven Universitair Fonds (B.D.S. and D.R.T.). This research was funded in whole or in part by European Research Council (ERC) under the European Union's Horizon 2020 Research and Innovation Programme (grant no. 834682), a cOAlition S organization. We will make the author accepted manuscript (AAM) version available under a CC BY public copyright license. **Author contributions:** D.R.T., M.J.K., S.B., and B.D.S. conceptualized the study design. M.J.K., Z.C.-V., and S.M. performed behavioral tests in mice. M.J.K. and S.M. performed neuropathological analyses, histological staining, mouse experiments, and statistical analysis. A.R. was responsible for breeding of the mice and mouse experiments. S.O. carried out histological staining and mouse experiments. S.R. and M.S. generated the APP23 and TAU58 transgenic and double transgenic mice and provided mouse brains of untreated animals for all genotypes. S.B. and D.T. carried out the cell culture experiments. M.J.K., S.M., and D.R.T. performed microscopic and quantitative analysis, data interpretation, and statistical analysis for all mouse experiments. S.B. and B.D.S. analyzed and interpreted all cell culture experiments and contributed to data interpretation. Visual documentation of the results was carried out by M.J.K., S.M., Z.C.-V., D.R.T., and S.B. Funding for this study was acquired by D.R.T., B.D.S., and S.B. M.J.K., S.M., D.R.T., A.R., S.O., Z.C.-V., S.R., M.S., D.T., S.B., and B.D.S. wrote and edited the paper. **Competing interests:** S.R. is and M.S. was an employee of Novartis Pharma (Basel Switzerland). B.D.S. has consulted for Eli Lilly, Biogen, Janssen Pharmaceutica, Eisai, and AbbVie. B.D.S. is also a scientific founder of Augustine Therapeutics and a scientific founder and stockholder of Muna Therapeutics. D.R.T. received speaker honoraria from Novartis (Switzerland) and Biogen (USA) and travel funds from GE Healthcare (UK) and UCB (Belgium) and has collaborations with Novartis Pharma AG (Switzerland), Probiodrug (Germany), GE Healthcare (UK), and Janssen Pharmaceutical Companies (Belgium). **Data and materials availability:** All data associated with this study are present in the paper or the Supplementary Materials. APP23 and TAU58 mice were used under a material transfer agreement (MTA) with Novartis Pharma (Basel, Switzerland). App^{NL-G-F} mice were provided by T. Saido under an MTA with RIKEN Institute. TAU-22 mice were provided by L. Buée (Lille Neuroscience & Cognition, Inserm UMR1172, France). Human postmortem brain tissue was obtained from the UZ/KU Leuven Biobank after approval of the project by the UZ/KU Leuven ethical committee (S-64378). MC1 antibody was provided by the P. Davies lab under an MTA with Albert Einstein College.

Submitted 26 October 2022
Resubmitted 7 November 2023
Accepted 10 October 2024
Published 30 October 2024
10.1126/scitranslmed.adf5128